AGU PUBLICATIONS

JGR

Journal of Geophysical Research: Earth Surface

RESEARCH ARTICLE

10.1002/2016JF003983

Key Points:
- Spatial and temporal variations of subsurface moisture content shown by long-term resistivity monitoring
- Long-term resistivity monitoring study implementing electrode movements on an active landslide
- Field validation of the impact of elevated pore pressures and preferential flow on slope stability

Supporting Information:
- Supporting Information S1

Correspondence to:
S. Uhlemann,
suhl@bgs.ac.uk

Citation:
Uhlemann, S., J. Chambers, P. Wilkinson, H. Maurer, A. Merritt, P. Meldrum, O. Kuras, D. Gunn, A. Smith, and T. Dijkstra (2017), Four-dimensional imaging of moisture dynamics during landslide reactivation, *J. Geophys. Res. Earth Surf.*, *122*, 398–418, doi:10.1002/2016JF003983.

Received 7 JUN 2016
Accepted 27 DEC 2016
Accepted article online 30 DEC 2016
Published online 25 JAN 2017

©2016 British Geological Survey (NERC).

Four-dimensional imaging of moisture dynamics during landslide reactivation

Sebastian Uhlemann[1,2], Jonathan Chambers[1], Paul Wilkinson[1], Hansruedi Maurer[2], Andrew Merritt[3], Philip Meldrum[1], Oliver Kuras[1], David Gunn[1], Alister Smith[4], and Tom Dijkstra[1]

[1]British Geological Survey, Nottingham, UK, [2]ETH Zurich, Institute of Geophysics, Zurich, Switzerland, [3]School of Geography, Earth and Environmental Sciences, Plymouth University, Plymouth, UK, [4]School of Civil and Building Engineering, Loughborough University, Leicestershire, UK

Abstract Landslides pose significant risks to communities and infrastructure, and mitigating these risks relies on understanding landslide causes and triggering processes. It has been shown that geophysical surveys can significantly contribute to the characterization of unstable slopes. However, hydrological processes can be temporally and spatially heterogeneous, requiring their related properties to be monitored over time. Geoelectrical monitoring can provide temporal and volumetric distributions of electrical resistivity, which are directly related to moisture content. To date, studies demonstrating this capability have been restricted to 2-D sections, which are insufficient to capture the full degree of spatial heterogeneity. This study is the first to employ 4-D (i.e., 3-D time lapse) resistivity imaging on an active landslide, providing long-term data (3 years) highlighting the evolution of moisture content prior to landslide reactivation and showing its decline post reactivation. Crucially, the time-lapse inversion methodology employed here incorporates movements of the electrodes on the unstable surface. Although seasonal characteristics dominate the shallow moisture dynamics during the first 2 years with surficial drying in summer and wetting in winter, in the months preceding reactivation, moisture content increased by more than 45% throughout the slope. This is in agreement with independent data showing a significant rise in piezometric heads and shallow soil moisture contents as a result of prolonged and intense rainfall. Based on these results, remediation measures could be designed and early-warning systems implemented. Thus, resistivity monitoring that can allow for moving electrodes provides a new means for the effective mitigation of landslide risk.

1. Introduction

Landslides cause severe societal and economic impacts globally each year. Between 2007 and 2015, more than 7200 landslides were recorded worldwide, causing more than 26,000 fatalities and exceeding damage costs, i.e., direct impact, of $1.8 billion [*Kirschbaum et al.*, 2015; *Guha-Sapir et al.*, 2016]. During the same 8 year period, 759 landslides were recorded in the UK [*Pennington et al.*, 2015] with more than half of these occurring in 2012/2013 after an exceptionally wet year [*Belcher et al.*, 2014]. Their economic impact, especially on the UK's infrastructure, is considerable [*Dijkstra and Dixon*, 2010; *Gibson et al.*, 2013; *Dijkstra et al.*, 2014; *Glendinning et al.*, 2015]; network disruptions caused by earthwork failures in 2012/2013 accounted for more than $10 M of compensation costs alone [*Network Rail*, 2014]. Infiltration of rainfall is a dominant factor triggering landslides [*Gasmo et al.*, 2000; *Highland and Bobrowsky*, 2008], and risk mitigation strategies therefore frequently implement hydrological and ground movement monitoring. These monitoring efforts are often aimed at understanding movement patterns and potential rainfall thresholds [*Malet et al.*, 2002; *Mora et al.*, 2003; *Corsini et al.*, 2005; *Simeoni and Mongiovì*, 2007; *Smith et al.*, 2014] in order to provide early warning to vulnerable communities and assets [*Michoud et al.*, 2013]. During the last 20 years, geophysical surveying has frequently been applied to the characterization of landslide structures [*Jongmans and Garambois*, 2007], but geophysical monitoring studies aiming to understand the actual hydrological and geotechnical processes causing failure are still sparse [*Perrone et al.*, 2014]. However, such efforts would enable changes in the subsurface conditions to be imaged prior to the onset of strains, rather than conventional approaches that only allow for observing their results.

Soil moisture and pore water pressure are controlling parameters on the effective stress and shear strength in slopes [*Bishop and Bjerrum*, 1960; *Springman et al.*, 2003; *Lu et al.*, 2010]. Hence, imaging the spatial and temporal distributions of these parameters together with movement and rainfall data aids in obtaining a detailed understanding of landslide characteristic processes [*Lehmann et al.*, 2013; *Springman et al.*, 2013;

Bordoni et al., 2015]. Due to the soil and geological characteristics of landslide deposits, these distributions can be highly heterogeneous [*Malet et al*., 2005]; thus, soil moisture and pore pressure recorded by conventional point sensors can provide high temporal resolution data at distinct points but are usually insufficient to image these complexities.

Geophysical monitoring can overcome this limitation by providing time series of volumetric data. The most frequently applied geophysical technique to image hydrological processes, for landslides in particular, is electrical resistivity imaging (ERI) [*Perrone et al*., 2014; *Binley et al*., 2015]. This technique employs measurements of electrical potentials at discrete locations and times on the surface and/or in boreholes that result from an active application of electrical current. ERI produces volumetric images of the resistivity of Earth materials which is, along with other factors, highly sensitive to changes in moisture content and so can be used to image subsurface moisture dynamics [e.g., *Schwartz et al*., 2008; *Brunet et al*., 2010].

Recently, various studies have shown that ERI monitoring is capable of imaging moisture movements in landslides. *Lehmann et al*. [2013] employed 2-D ERI to image moisture movements within a slope under stable and unstable conditions. Their results showed very good correlation between conventional point sensors and ERI-derived moisture estimates and demonstrated that ERI monitoring can be used to define the spatial and temporal evolution of saturation in unstable slopes. *Supper et al*. [2014] presented short-term (hourly) and long-term (monthly) 2-D ERI monitoring from two alpine landslides, highlighting the correlation between landslide activity and decreasing resistivities due to increasing moisture contents. *Gance et al*. [2016] concluded from their ERI results that rainfall infiltration changed not only the soil moisture content but also the temperature in the near surface. So far, however, ERI monitoring studies have been limited to 2-D cross sections parallel or perpendicular to the landslide movement direction.

Although 2-D investigations can monitor moisture movement along predefined transects, they are not able to address the full spatial heterogeneity of moisture dynamics in landslides. Our study overcomes this limitation for the first time by employing 3-D ERI monitoring to image the moisture dynamics of an active landslide prior to reactivation and post reactivation. Another important advance is that this is the first ERI monitoring study to incorporate electrode displacements into the time-lapse inversion workflow. When landslides move, the electrode positions vary with time. Several studies have shown that misplaced electrodes cause significant distortions in the resistivity models [*Zhou and Dahlin*, 2003; *Oldenborger et al*., 2005; *Szalai et al*., 2008; *Wilkinson et al*., 2008, 2010, 2015, 2016; *Uhlemann et al*., 2015]. At the studied landslide, *Uhlemann et al*. [2015] showed that the downslope movement of mass and electrodes of up to 2.9 m (equal to 60% of the electrode spacing) caused artifacts in the resistivity models that changed the imaged resistivities by more than 40% (Figure 1). The magnitudes of these distortions were likely to exceed and thus mask any resistivity changes caused by subsurface moisture variations. Hence, we present a novel methodology that incorporates changing electrode locations into the time-lapse inversion methodology, which enables imaging of moisture dynamics in actively moving landslides. This methodology is applied to an extensive 4-D ERI data set spanning more than 2 years and is analyzed together with conventional monitoring data (i.e., soil moisture, piezometric heads, and deformation), providing new insights into the reactivation of slow-moving landslides. This new capability is a crucial improvement required for the integration of ERI monitoring in landslide early warning systems.

2. The Hollin Hill Landslide Observatory

2.1. Geological and Geomorphological Setting

Mudstone formations of the Lower Jurassic (Lias group) are some of the most susceptible to inland landslides in the UK, exhibiting a landslide density of up to 42 per 100 km^2 of outcrop [*Hobbs et al*., 2012]. The study site, Hollin Hill, is located on a south facing slope at the southern edge of the Howardian Hills in North Yorkshire, UK, and comprises a succession of four shallow marine mudstone-dominated units of Lower and Middle Jurassic age (Figure 2). In ascending order these are the Redcar Mudstone (RMF), Staithes Sandstone and Cleveland Ironstone (SSF), Whitby Mudstone (WMF), and Dogger Formation (DF). In the region, the surficial deposits are characterized by highly heterogeneous and poorly compacted sediments that are prone to landsliding, which is a consequence of repeated slope instabilities interpreted to have occurred during the last glaciation in the Pleistocene. These instabilities were caused by water-level dynamics of an ice-marginal lake, Lake Mowthorpe (Figure 2a). The DF shows considerable variation in thickness and lithology but locally forms an up

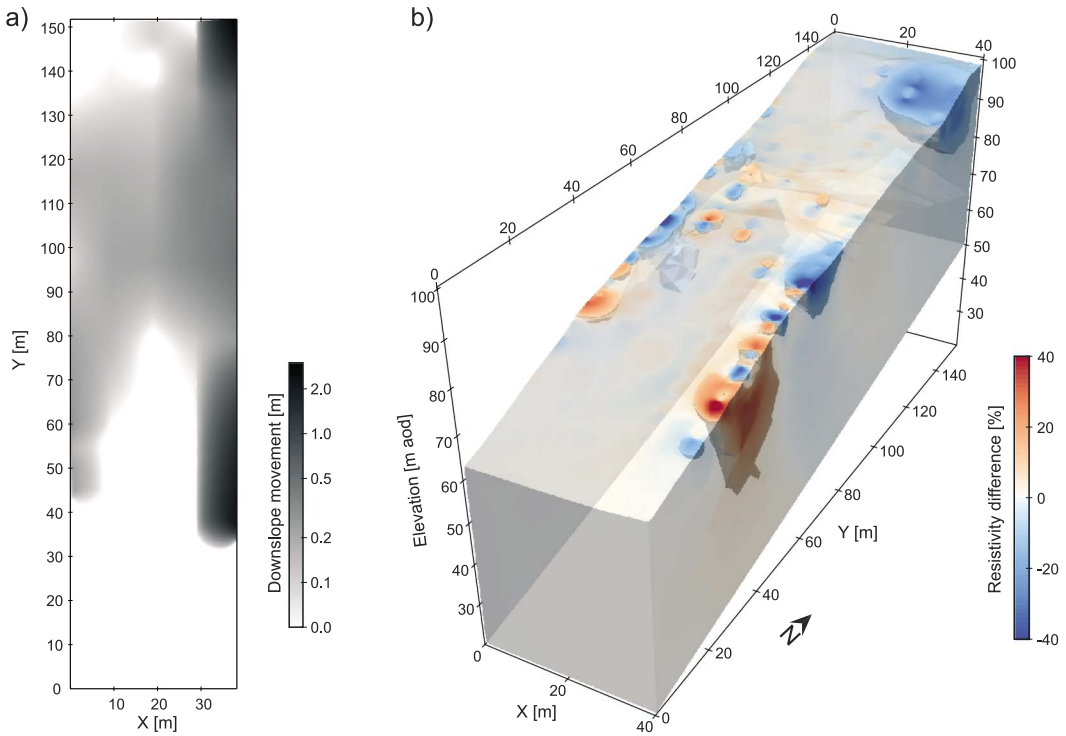

Figure 1. Effects of electrode movements on the inverted resistivity model (adapted from *Uhlemann et al.* [2015]): (a) map showing typical surficial downslope mass movements at the study site over a period of >2 years, measured using repeat GPS surveys of benchmark positions, and (b) volumetric model showing resistivity artifacts occurring when inverting data without correcting for electrode movements. Elevations are above ordinance datum (AOD).

to 8 m thick limestone- and sandstone-dominated unit. It represents a potentially perched aquifer above the poorly drained bluish grey to dark-grey mudstones and siltstones of the WMF [*Foster et al.*, 2007]. The WMF is the failing formation at the site and is a particularly landslide-prone formation in the region and throughout the UK [*Foster et al.*, 2007; *Hobbs et al.*, 2012]. The landslides indicated in Figure 2a are all located in outcropping WMF. Underlying the approximately 25 m thick WMF is the SSF, which is formed of ferruginous, micaceous siltstone with fine-grained sandstone and thin mudstone partings and is heavily bioturbated [*Gaunt et al.*, 1980]. The SSF is the main aquifer at site. It has a thickness of about 20 m and is associated with well-drained loam soil in the middle and lower part of the slope. The boundary between WMF and SSF is lithologically gradational and involves a transition from poorly drained material of the WMF to relatively well drained material of the SSF. This has been observed in several auger and boreholes and in a recent seismic study [*Uhlemann et al.*, 2016b]. The lower boundary of the SSF shows a gradational change to poorly drained grey, silty mudstones of the RMF and is expressed as a spring line at the toe of the slope (Figure 2b). A thin layer of head deposits (0.2–1.3 m thick) overlays the bedrock succession. These head deposits are characterized by gravelly, sandy, and silty clay with occasional organic inclusions, mainly derived from the DF by a combination of geomorphological processes such as hillwash, slope failure, and soil creep [*Chambers et al.*, 2011; *Uhlemann et al.*, 2016a]. The lower slope is covered by clayey, fine sand deposits (up to 2 m thickness), which are interpreted as aeolian sands [*Uhlemann et al.*, 2016b].

After *Cruden and Varnes* [1996], the landslide can be classified as a very slow to slow moving composite multiple Earth slide/flow. In recent years, movement rates of up to 3.5 m/yr have been observed. The main driver of mass movement processes are translational movements in the central part of the WMF. These translational movements toward the WMF-SSF boundary evolve to slide/flow-like movements that form lobes toward the toe and drive rotational failures in the upper slope [*Uhlemann et al.*, 2016a]. The ERI monitoring area is set between two of these lobes (Figure 2b), referred to as eastern and western lobes hereafter. Reactivation of landslide activity is controlled by the saturation state of this domain, with wetting predominantly taking place through direct infiltration following prolonged and intense rainfall, and assisted by

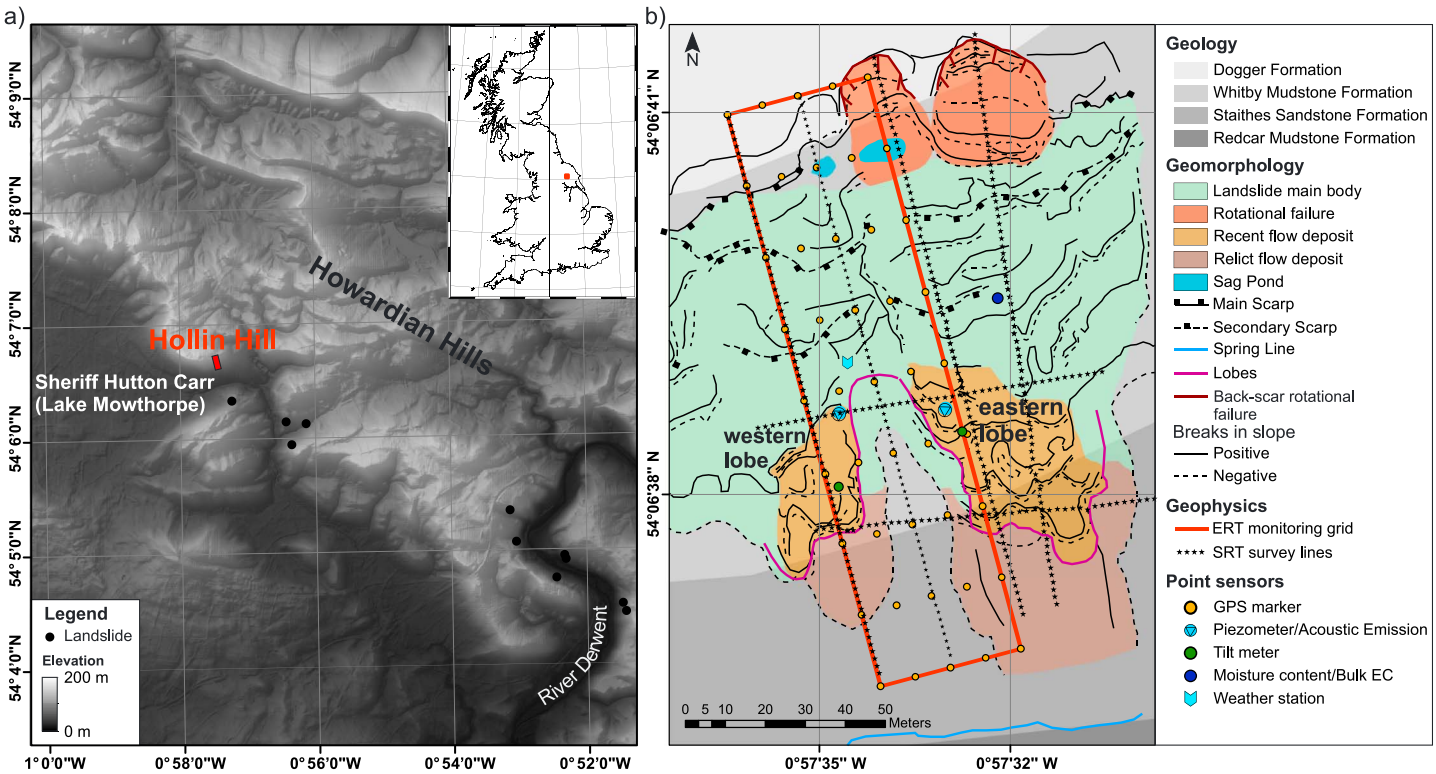

Figure 2. (a) Digital elevation model (DEM) of the study region and recent landslide locations; inset shows the location of the study site in the UK. Note that all landslides are located in outcropping WMF. (b) Geology, geomorphology, and instrumentation are highlighted on a plan of the study site. The geomorphological map is modified after *Merritt et al*. [2013].

groundwater inflow from the DF [*Uhlemann et al*., 2016b]. Elevated soil moisture and pore water pressures in the existing lobes lead to reactivation of shear strains along preexisting shear surfaces at critical depths of around 2–3 m; in the back scarp elevated soil moisture and pore water pressures can lead to activation of shear strains along newly developing shear surfaces at similar depths. Thin aeolian sand deposits overlying the SSF potentially act as a toe drain to the sliding material, causing a deceleration of movements and the buildup of ridges along the slope. Lobes are formed by slide/flow-like movement as a consequence of a local breakthrough after repeated phases of deformation, leading to a rapid acceleration of low shear strength material. The ongoing deformations of the translation-dominant domain cause a loss of support of the local toe of the upper slope, triggering retrograding shallow rotational failures. A more detailed discussion of the geomorphological processes defining the landslide activity at Hollin Hill can be found in *Uhlemann et al*. [2016a, 2016b].

2.2. Landslide Characterization: Geophysical and Geotechnical Approaches

Hollin Hill acts as a field laboratory for landslide research with a remit for technological and methodological developments in acoustic emission and ERI for landslide monitoring and early warning [*Wilkinson et al*., 2010, 2016; *Dixon et al*., 2014; *Smith and Dixon*, 2015; *Uhlemann et al*., 2015]. It has been well characterized using geological and geomorphological mapping [*Merritt et al*., 2013], geotechnical investigations [*Gunn et al*., 2013] and monitoring [*Smith et al*., 2014; *Uhlemann et al*., 2016a], and geophysical characterization [*Chambers et al*., 2011; *Uhlemann et al*., 2016b]. ERI monitoring data acquired at site were the driver for recent developments in resistivity-derived [*Wilkinson et al*., 2010, 2016] and GPS-interpolated [*Uhlemann et al*., 2015] tracking of electrode movements. These developments are an essential prerequisite for the work presented here.

As a field laboratory, Hollin Hill is equipped with a range of monitoring devices, including continuously logged piezometers, tiltmeters, acoustic emission active waveguides (AEWGs), multiparameter sensor nodes measuring gravimetric moisture content (GMC), bulk electrical conductivity, and temperature, as well as a

weather station. In addition, a grid of GPS benchmarks is surveyed periodically using RTK-GPS equipment to measure and define mass movements at the ground surface. Piezometers, tiltmeters, and AEWG are installed on the two lobes, recording data of the most active parts of the landslide. Piezometers are installed to depths of 2.25 m and 2.45 m below ground level (bgl) in the western and eastern lobes, respectively. The lower 0.5 m acts as the active zone of these piezometers, with their tops being located just below the sliding surface, which was determined using cone penetration resistance measurements [*Gunn et al*., 2013]. Thus, the recorded piezometric head is indicative of the pore pressures at the sliding surface; piezometric heads above the top of the active zone correspond to positive pore water pressure at the sliding surface, while piezometric heads below the top of the active zone similarly correspond to negative pore pressures. Multiparameter sensors, measuring soil temperature, moisture content, and bulk resistivity, are installed as clusters of five sensors each distributed over depth, with sensors located between 0.1 and 6.4 m bgl. These clusters are located at the back scarp, lobe, and toe region to provide representative data of the entire landslide and its different lithologies. The sensor locations are shown in Figure 2b.

The field geophysical characterization of the study site has been based on geoelectrical methods, i.e., ERI, resistivity, and self-potential mapping [*Chambers et al*., 2011] and seismic refraction tomography [*Uhlemann et al*., 2016b]. These surveys have been successful in imaging the different lithologies and landslide domains of the site, providing a clear indication of the boundary between WMF and SSF and the extent of the lobes. They also highlighted the different moisture characteristics of these domains; while the WMF shows generally very high moisture content, the SSF is characterized by significantly lower saturation levels. In the seismic results, this was indicated by high and low values for the Poisson's ratio, respectively. The electrical resistivity of the formations is also considerably different; the WMF, due to its high clay and moisture content, has a markedly lower resistivity ($<30\,\Omega$m) than the underlying, more silt/sand-rich SSF ($>30\,\Omega$m).

2.3. Landslide Reactivation During Winter 2012/2013

The landslide reactivated in the winter of 2012/2013, after a period of about 2 years without significant movements (Figure 3a). This reactivation was caused by two consecutive wet summers, with the summer of 2012 being the wettest in the last century [*Pennington and Harrison*, 2013; *Belcher et al*., 2014], leading to a continuous rise of the piezometric head and thus pore pressures close to a preexisting slip surface. Triggering of movements can be related to prolonged intense rainfall that occurred in the winter of 2012/2013, which regionally accumulated 50% above the 30 year average [*Belcher et al*., 2014]. At the study site this resulted in the highest effective rainfall recorded over the monitoring period, where effective rainfall is defined as actual rainfall minus potential evapotranspiration. While movements at the toe of the eastern lobe commenced slowly between July and October 2012, a rapid acceleration of lobe movements was recorded between December 2012 and January 2013. This latter acceleration also coincided with a rotational failure that occurred at the eastern edge of the ERI monitoring array (Figure 2b). Although activity was recorded at the western lobe (tiltmeter readings in Figure 3b), these commenced past the activation of the eastern lobe and showed significantly smaller amplitude (benchmark movement in Figure 3a). In May 2013, pore pressures returned to a level characteristic of the period prior to the reactivation. Thus, landslide activity and lobe movements significantly decreased.

Rainfall is known to be the fundamental triggering mechanism for landslide activity at this site. Prolonged and intense rainfall leads to increasing pore pressures in the subsurface, causing an acceleration of movements [*Uhlemann et al*., 2016a]. The dissipation of pore pressures then leads to a deceleration of movements, as shear strength and effective stress increase. This sequence results in an "*S*"-shaped movement characteristic of the Hollin Hill landslide, which can be observed over long and short terms (Figure 3b) and has been observed at several landslides [*Allison and Brunsden*, 1990; *Petley et al*., 2005; *Smith et al*., 2014].

3. Geoelectrical Monitoring Methodology

3.1. Field Installation

Installed in March 2008, the 3-D ERI monitoring installation consists of 5 parallel lines of 32 electrodes each, with 4.75 m electrode spacing and 9.5 m interline spacing. The installation forms a rectangular grid of 160 electrodes, with the dimensions of approximately 147 m × 38 m (Figure 2b). These dimensions and spacing were chosen in order to monitor the resistivity dynamics of the entire slope, centered on two actively moving lobes. It allows for the comparison of moisture dynamics in different movement domains. Electrodes were

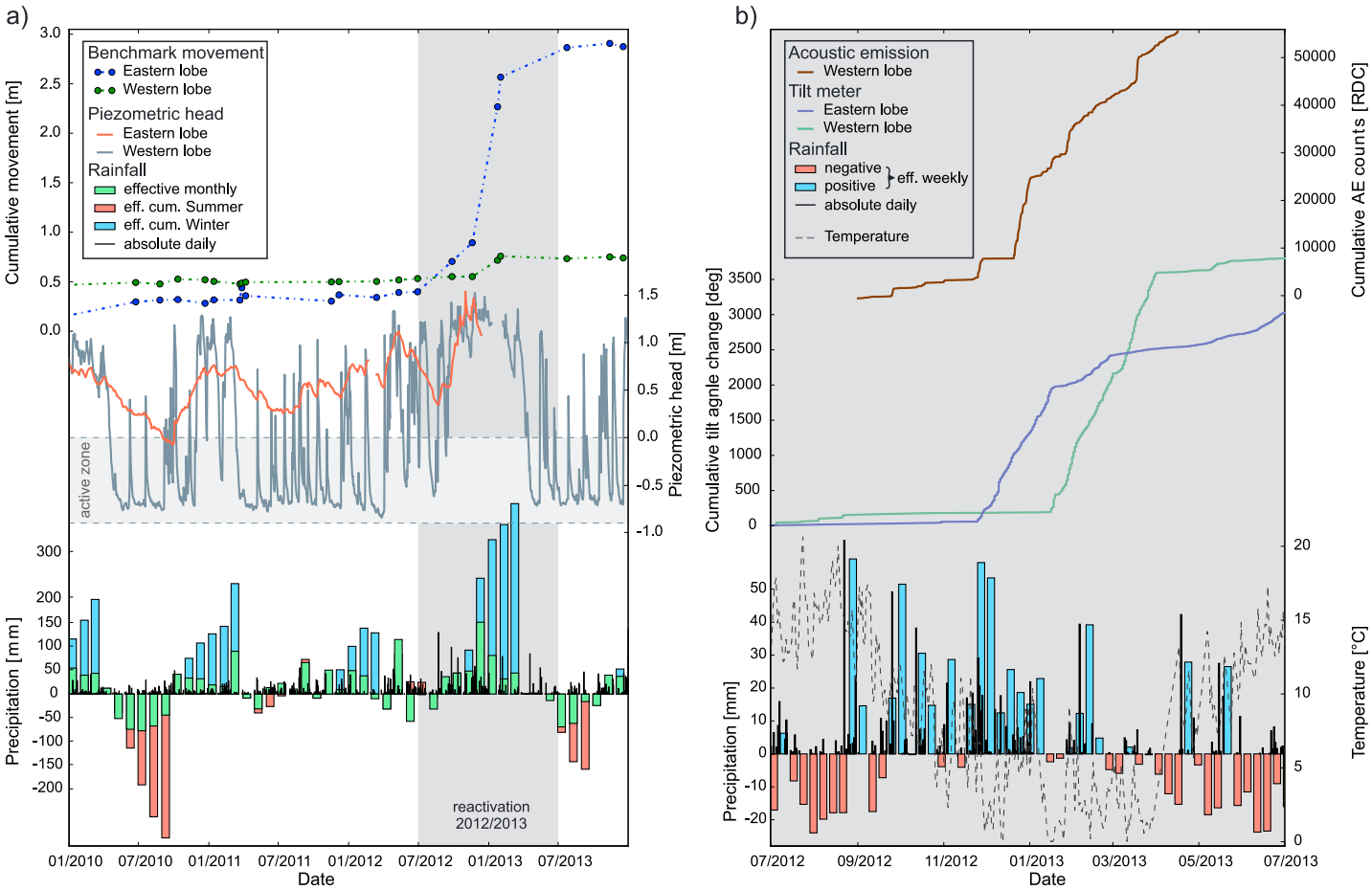

Figure 3. (a) Movement, piezometric head, and rainfall data for 2010–2013. (b) The period of reactivation is highlighted. Benchmark movements shown in Figure 3a correspond to repeated RTK-GPS measurements of benchmarks installed toward the toe of the lobes. The active zone shown for the piezometric head indicates the screened area. Note that the upper end of this zone corresponds to an existing slip surface. Cumulative effective rainfall data show a clear indication of two consecutive wet summers in 2011 and 2012, followed by an exceptionally wet winter of 2012/2013. The tiltmeter and acoustic emission data in Figure 3b show the "*S*"-shaped activity of the landslide, where increasing pore pressures result in an increase in activity, followed by decreasing pore pressures causing a decrease in activity. Subsets of these data series are discussed in detail in *Uhlemann et al.* [2016a].

installed in shallow trenches about 0.1 m bgl and backfilled to avoid damage from animals and other site activities. Electrode locations were surveyed using RTK-GPS equipment during installation. At the same time, GPS benchmarks were installed and repeatedly surveyed throughout the monitoring duration. The movement data obtained from these measurements were used to estimate the electrode movement [*Uhlemann et al.*, 2015] and provided a time series of electrode locations employed in the ERI inversion.

Automated ERI monitoring commenced in January 2009 and is still ongoing. Using an automated time-lapse electrical resistivity tomography measurement system [*Kuras et al.*, 2009], data were collected on alternating days (with occasional data gaps due to system, power, or telemetry failures). The measurement sequence comprised conventional dipole-dipole measurements, using dipole lengths a of 4.75–19 m and dipole separations na with $n = 1$–8. Each of the 2580 apparent resistivity measurements was made in normal ρ_n and reciprocal configuration ρ_r [*LaBrecque et al.*, 1996], with the measured value being defined as the mean of these two measurements ρ_m. The measurement error e was defined as the percentage standard error in the mean, which is referred to as the reciprocal error, defined as

$$|e| = 100 \cdot \left(\frac{|\rho_r - \rho_n|}{(\rho_r - \rho_m)} \right). \tag{1}$$

Data were filtered out based on three criteria: (1) having negative apparent resistivity, (2) having a reciprocal error of more than 10%, and (3) having a positive/negative pulse amplitude ratio outside the range of

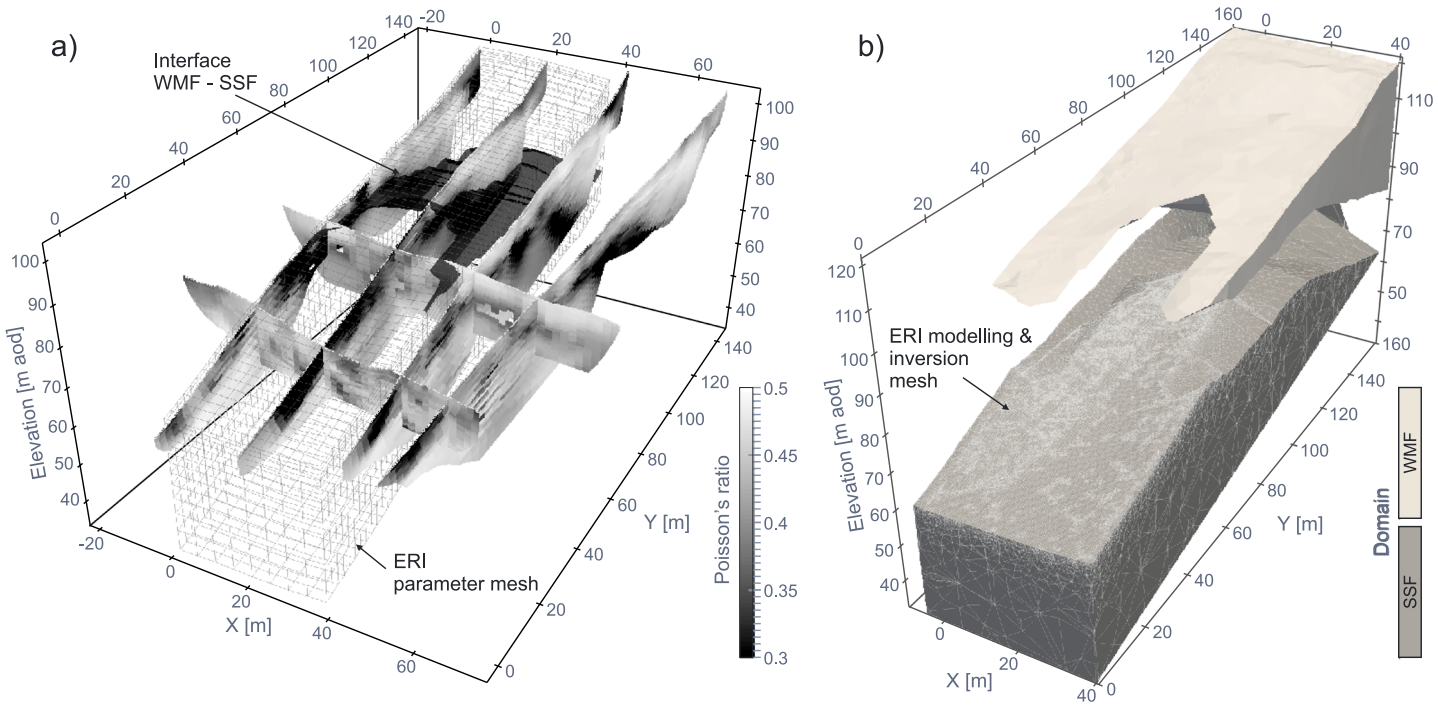

Figure 4. (a) Poisson's ratio as derived from *P* and *S* wave SRT by *Uhlemann et al*. [2016b]. The interface between WMF and SSF (black surface) was extracted based on the largest negative gradient of the Poisson's ratio with depth. Note that the SSF exhibits considerably lower Poisson's ratio than the overlying, poorly drained WMF. (b) Mesh used for ERI forward modeling and inversion; the mesh has been divided into two domains, representing WMF and SSF, respectively. The WMF domain has been raised by 20 m to show the boundary between the domains. The parameter mesh is shown in Figure 4a.

0.85–1.15 (a measure of waveform symmetry). Data quality varied throughout the monitoring period, typically with decreasing data quality in summer, due to increasing contact resistances, and improving in winter. Generally, more than 85% of the data remained after filtering.

3.2. Seismic Data as Structural Constraint

In a previous study, *Uhlemann et al*. [2016b] presented shallow *P* and *S* wave seismic refraction tomography data acquired at Hollin Hill. The elastic moduli derived from the *P* and *S* wave velocities indicated small shear strength of the materials in the failing domains, while the Poisson's ratio, due to its sensitivity to water saturation [*Huang et al*., 2012], provided a clear indication of the boundary between the WMF and the SSF (Figure 4a). This boundary was extracted from the Poisson's ratio by calculating the gradient along the *z* direction and defining the WMF-SSF interface as the depth of the largest negative gradient. To allow this boundary to be included in the ERI forward modeling and inversion mesh, it was simplified by only using those points that reflected a significant change of the interface direction. The interface showed a local 5–8° dip toward the north, which is in agreement with previous studies [*Merritt et al*., 2013], and it reflects the two lobes at the western and eastern edge of the study area (Figure 4).

Combining different geophysical techniques and including a priori information into ERI inversion is known to reduce uncertainties [*Loke et al*., 2013] and improve the information content that can be derived from surface geophysical methods [*Doetsch et al*., 2012]. Recently, *Bergmann et al*. [2014] and *Benisch et al*. [2015] have reported an improved resolution for ERI monitoring studies, when the ERI inversion was constrained by a priori structural information obtained from seismic data. In this study, structural constraints were included in the ERI inversion by dividing the mesh at the WMF-SSF interface into two domains, comparable to *Doetsch et al*. [2012], who combined ground-penetrating radar and ERI data. This division is justified as the unsaturated resistivity of the SSF has been determined in the laboratory to be significantly higher than the resistivity of the WMF [*Merritt et al*., 2016]. Field observations have also shown that moisture content considerably decreases at the WMF-SSF interface, amplifying the resistivity difference.

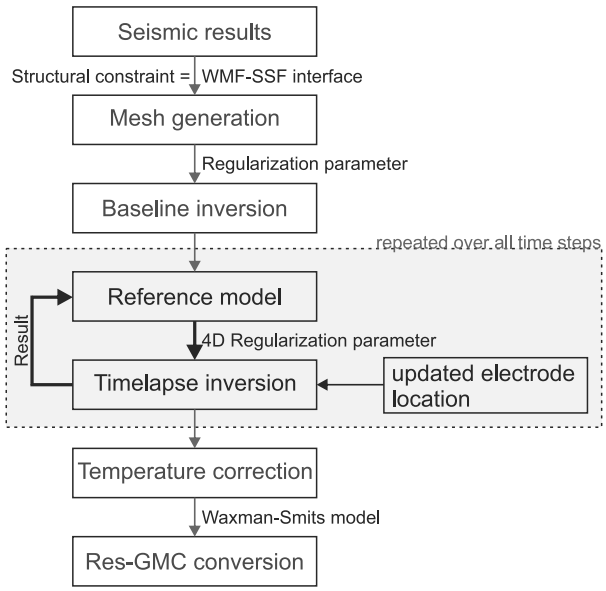

Figure 5. Time-lapse inversion workflow. Structural constraints are implemented in the mesh generation, where the WMF and the SSF are defined as separate domains, and subsequently different regularization constraints are assigned. Within the time-lapse workflow, each inversion is constrained to the resistivity model of the previous time step and employs the electrode locations of the corresponding date. All resistivity models are temperature corrected, and resistivities are converted to gravimetric moisture content (GMC).

To invert the resistivity data the fully parallelized inversion code "*E4D*" was used [*Johnson et al.*, 2010]. It allows the implementation of structural constraints in different ways: (1) by defining different regularization parameters for each domain, (2) by placing constraints on the model cells along the boundary, and (3) by omitting weights from cells of another domain, thereby "decoupling" the two inversion domains (Figure 4b). While the resistivity of the two formations is known to be different, their variability is assumed to be similar and smooth. Thus, a conventional L2 norm was applied to each inversion domain. Different weights for constraining the model across the boundary were tested; the best results were obtained when applying smoothness constraints across the boundary with small relative weight (0.1 for smoothness across boundary and 1.0 for independent domain constraints).

3.3. The 4-D Inversion Workflow

While it is well known that inaccurate electrode positions lead to severe artifacts in the inverted resistivity models [*Zhou and Dahlin*, 2003; *Oldenborger et al.*, 2005; *Szalai et al.*, 2008; *Wilkinson et al.*, 2008, 2010, 2015], conventional time-lapse inversion methodologies, such as difference, ratio, or 4-D inversion [e.g., *LaBrecque and Yang*, 2001; *Daily et al.*, 2004; *Kim et al.*, 2009], have not previously allowed for changing electrode positions with time. Thus, a new methodology has been developed to incorporate electrode movements into a time-lapse inversion workflow (Figure 5). This methodology relies on constraining the inversion of a single time step against a reference model obtained from a previous time step or baseline measurement, similar to what has been proposed by *Loke* [2001].

The resistivity model obtained from the structurally constrained inversion of a baseline data set forms the reference model for the inversion of the data of the first time step. For the following time steps the inverted resistivity model of the previous time step is used as reference. As resistivity changes were expected to vary smoothly with time, an L2 norm was applied to the temporal changes, which caused the changes in resistivity between adjacent temporal models to be smooth in time [*Loke et al.*, 2014]. The relative weights of spatial and temporal constraints were defined as 0.8 and 0.2, respectively. Thus, spatial smoothness is favored over temporal smoothness. These values were chosen as they provided the best results: applying stronger temporal constraints led to overly smooth changes in time, whereas smaller temporal constraints led to artifacts, especially in deeper parts of the model. At each iteration the global constraint weighting was reduced if the reduction in the objective function was small, leading to faster convergence [*Johnson et al.*, 2010]. Note that the inversion mesh is created only once and used for all time steps. This assumes that changes in surface topography are comparatively small and have a negligible effect on the resistivity model [*Wilkinson et al.*, 2015]; a constant mesh is a prerequisite for the temporally constrained inversion.

The ERI time series covers 43 months, starting from January 2010 and ending in July 2013. This period was chosen as it covers seasonal variations and intense rainfall leading to the reactivation of instabilities and provides information about moisture dynamic post reactivation. Only a subset of the entire recorded data was used in this series to study the seasonal processes (analyzing all the data would have been too computationally

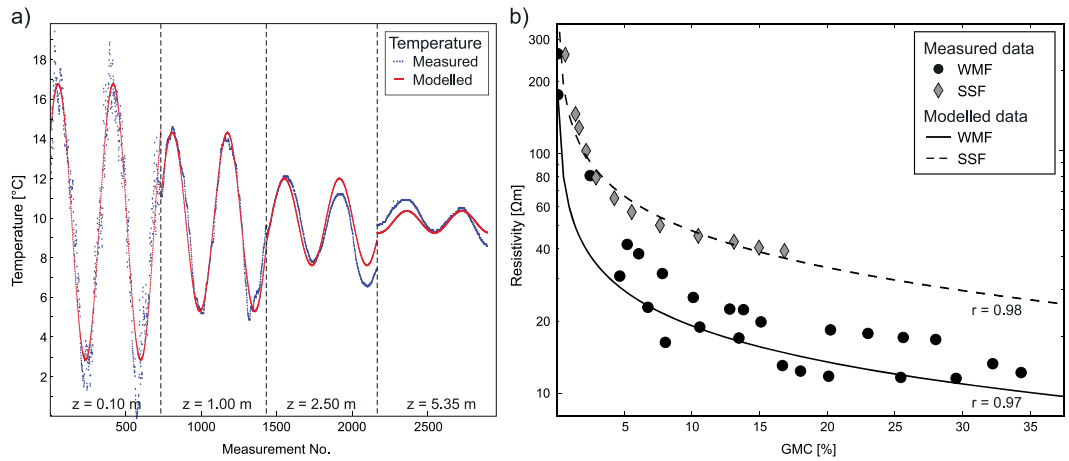

Figure 6. (a) Temperature model (red) fitted to multilevel temperature data (blue dots) acquired over a period of 2 years. (b) GMC-resistivity relationship for the two main formations determined from laboratory measurements and fitted by Waxman-Smits models.

demanding). Thus, the analyzed time series comprised 43 data sets, approximately one for each month of the monitoring period, considering data quality and availability (for acquisition dates and data characteristics, the reader is referred to Table S1 in the supporting information).

For the inversion of each time step, the electrode positions were updated using interpolation of GPS benchmark measurements [*Uhlemann et al.*, 2015]. Within the inversion, electrodes have to be placed at mesh nodes. To minimize spatial inaccuracies introduced by this limitation, a very fine discretization was applied at the surface (Figure 4b), with cells having volumes of less than 0.03 m^3 and node spacings of less than 0.5 m, what is significantly smaller than the surface displacements of up to 3.5 m. Thus, the difference between interpolated electrode position and used mesh node usually remained below 0.25 m, which is less than 6% of the electrode spacing, and below the accuracy of the interpolation method.

In each inversion the data were weighted by their corresponding reciprocal error, given that the error was above a lower limit of 10% the average noise level. This was calculated based on the data between the 10th and 90th percentiles in order to remove data outliers. This approach has previously been shown to provide robust inversion results, especially when applied to long-term data where error characteristics may change over time and frequently applied error models tend to underestimate data errors [*Uhlemann et al.*, 2016c]. A forward modeling error of 2% of the measured resistance was added to the reciprocal error. Each inversion converged at $\chi^2 = 1$, equal to a root-mean-squared misfit between measured and modeled data of 1.9 to 3.0% (for detailed information on inversion errors and number of iterations, the reader is referred to Table S1).

3.4. Conversion of Resistivity Data to Moisture Content

The electrical resistivity of Earth materials is sensitive to variations in temperature; above 0°C resistivity decreases linearly by about 2%/°C with increasing temperatures [*Hayley et al.*, 2007]. Seasonal temperature variations can introduce changes in the subsurface resistivities that are of the same order as changes caused by hydrological processes. Thus, resistivity models need to be corrected to a standard temperature to remove these seasonal variability and avoid misinterpretation of the resistivity monitoring data [*Chambers et al.*, 2014; *Chrétien et al.*, 2014].

Temperature data were acquired at depths of 0.1, 1.0, 2.5, and 5.35 m bgl over a period of 2 years. This multidepth temperature time series was used to fit a simplified temperature model describing the seasonal temperature variations in the subsurface (Figure 6a). The temperature model, which defines the temperature at depth z and day t, is based on the diffusive heat equation and is defined as [*Brunet et al.*, 2010]

$$T_{\text{model}}(z,t) = T_{\text{mean}} + \frac{\Delta T}{2}\exp\left(-\frac{z}{d}\right)\sin\left(\frac{2\pi}{365}t + \phi - \frac{z}{d}\right), \tag{2}$$

with the annual mean temperature T_{mean}, the peak-to-trough amplitude of the temperature variation ΔT, a characteristic depth d at which ΔT has decreased by $1/e$, and a phase offset φ to bring surface and air

Table 1. Parameters of the Waxman-Smits Model for the Two Formations[a]

Formation	F^b (m)	n^b (−)	Φ (%)	D_g (g/cm^3)	D_w (g/cm^3)	σ_w (S/m)	B_{ws} (S cm^3 m^{-1} meq^{-1})	c (meq/100 g)
WMF	17.43	1.47	45.0	2.69	1.00	0.0987	2.042	22.5
SSF	51.01	1.45	32.0	2.74	1.00	0.0987	2.042	11.0

[a]All parameters were determined by laboratory testing [*Merritt et al.*, 2016], except of F and n, which were obtained by fitting the model to laboratory GMC-resistivity data.
[b]Parameters obtained from fitting Waxman-Smits model to laboratory data.

temperature into phase. From the field data, we obtained $T_{\text{mean}} = 10.03°\text{C}$, $\Delta T = 15.54°\text{C}$, $d = 2.26$ m, and $\phi = -1.91$. Note that this methodology does not account for changes in thermal conductivity caused by changing subsurface saturation. Nevertheless, the model fits the data very well, having an RMS error of only 1.1%. This model was used to estimate the temperature at every cell of the resistivity model at each time step and subsequently to correct the model resistivities ρ to a standard temperature $T_{\text{standard}} = 20°\text{C}$ using the ratio model [*Hayashi*, 2004; *Ma et al.*, 2011], which can be written as

$$\rho_{\text{cor}} = \rho\left[1 + \frac{tc}{100}(T_{\text{standard}} - T_{\text{model}})\right] \tag{3}$$

with a temperature correction factor tc of $-2.0°\text{C}^{-1}$.

To translate the temperature-corrected resistivity models into gravimetric moisture content (GMC), laboratory work was undertaken to determine the relationship between these two soil properties [*Merritt et al.*, 2016]. The resistivity of borehole samples representative for WMF and SSF was measured at various GMC, during wetting and drying cycles. A Waxman-Smits model was fitted to each formations' data [*Waxman and Smits*, 1968] (Figure 6b). This electro-petrophysical model was chosen as it accounts for electrical conduction in the electrical double layer, which shows a significant contribution in clayey materials. In terms of GMC, the Waxman-Smits model can be defined as [*Chambers et al.*, 2014]

$$\rho(\text{GMC}) = F\left(\frac{(1-\varphi)D_g\text{GMC}}{\varphi D_w}\right)^{-n}\left(\sigma_w + B_{ws}\left[\frac{(1-\varphi)D_g c}{100\varphi}\right]\left[\frac{\varphi D_w}{(1-\varphi)D_g\text{GMC}}\right]\right)^{-1}, \tag{4}$$

with the formation factor F; the porosity Φ; the grain and water density D_g and D_w, respectively; the saturation exponent n; the pore water conductivity σ_w; the average mobility of the cations B_{ws}; and the cation exchange capacity c. All parameters, except for F and n, were determined from laboratory testing of the samples and are shown in Table 1. F and n were fitted from the data; for the two formations F was determined to be 17.43 and 51.01 m and n to be 1.47 and 1.45 for WMF and SSF, respectively. Using these parameters the model fits the data with a Pearson's correlation coefficient of $r = 0.97$ and 0.98 for WMF and SSF, respectively. Note that the sensitivity of resistivity to moisture content changes decreases with increasing moisture content.

Each resistivity model was translated into GMC using this Waxman-Smit model. The appropriate formation parameters were chosen based on the two domains of the inversion mesh. To reduce the calculation time required for the property translation and to ease visualization, the inversion mesh (1,083,789 cells) was translated to a parameter mesh (6448 cells; Figure 4a), only keeping the part of the inversion mesh which corresponds to the study area. This step increased cell sizes by about 4 times, from a node spacing of about 0.5 m to a node spacing of about 2.0 m for the inversion and parameter meshes, respectively.

4. Results

4.1. Material Characterization

Data acquired on 19 March 2010 were used as the baseline measurements. This date was chosen as it provided high-quality measurements (less than 1.5% of the data had reciprocal errors above 5%) acquired about 4 months after the landslide entered a 2 year period of stability. It is a characteristic data set for an intermediate saturation state of the slope; winters tend to be wetter, while summers are drier. The imaged resistivities show a clear indication of the formations present in the imaging volume (Figure 7a). The WMF, due to its high clay content (up to >50%), is characterized by low resistivity values, ranging between 5 and 30 Ωm. It overlies the sandier and thus more resistive SSF, with resistivities of more than 30 Ωm. The boundary between these

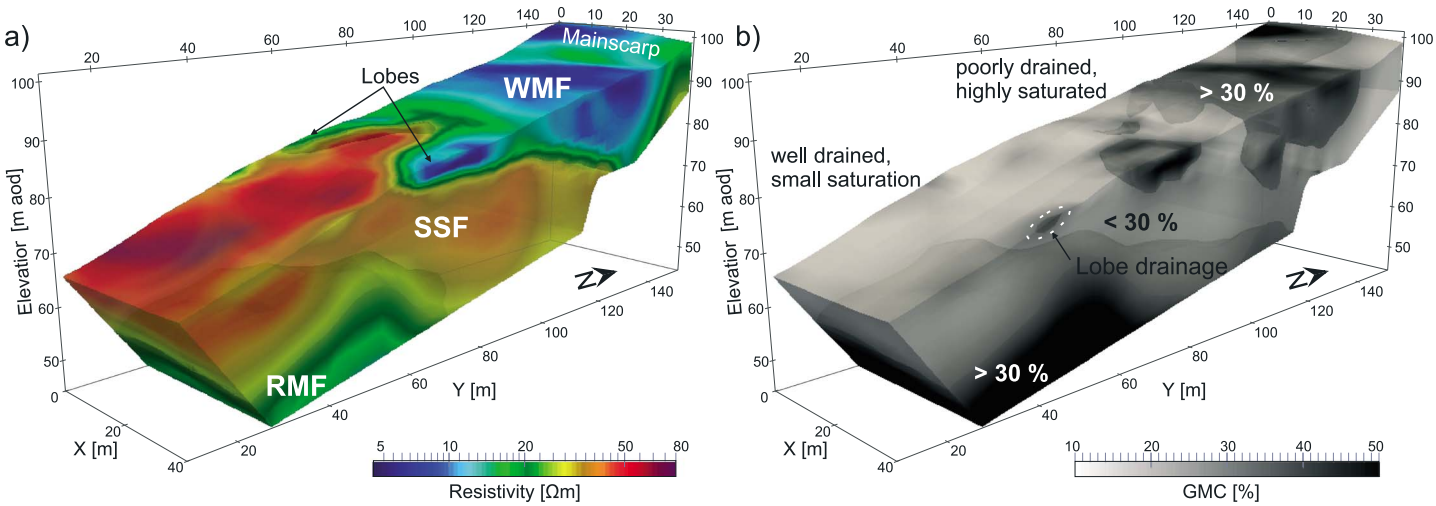

Figure 7. (a) Baseline resistivity and (b) derived GMC model. In the resistivity model areas of $\rho > 30\ \Omega$m are displayed opaque; areas with GMC $> 30\%$ are displayed opaque in the GMC model. The models derived from data acquired on 19 March 2010 are shown, a characteristic date of intermediate moisture levels. Only the imaging volume with a sensitivity $>1e-8$ is shown.

two formations is clearly imaged in the resistivity model, showing the local dip of the bedrock succession of about 5–8° to the north. The resistivity also provides a clear indication of the outline of the lobes, which can be seen as downslope thinning features protruding from the WMF on the eastern and western edge of the imaging volume. Note that despite including different domains in the inversion, resistivities change smoothly over these boundaries. For example, at the lobes the WMF mesh/inversion domain reaches further downslope (to about $y = 40$ m) than the conductive features extending from the WMF (to about $y = 60$ m; Figure 7a). The clay-rich RMF, which is outcropping further south of the imaging volume, is indicated in the southern part by resistivities below 30 Ωm at depths of more than 10 m bgl.

Translating resistivities into GMC highlights the different saturation characteristics of the WMF and SSF. While the majority of the WMF is characterized by moisture contents ranging between 25% and more than 60%, the SSF has a mean GMC of about 19% and remains nearly entirely below 30% (Figure 7b). As with the resistivities, the GMC distribution highlights the elevated moisture levels at the top of the eastern lobe in particular. Even small features, such as a frequently observed area of elevated moisture content at the toe of the eastern lobe where water drains at the interface between failed material and SSF, are captured in the image. At the WMF-SSF interface moisture levels decrease rapidly, which is in agreement with field observations from boreholes. The change in GMC over the SSF-RMF boundary is smoother. This is also in agreement with previous studies, where the lower part of the SSF was found to be under saturated condition [*Uhlemann et al.*, 2016b].

4.2. Moisture Dynamic Prereactivation

The imaged GMCs of 2010 and 2011 show a distinct seasonal behavior; while winter months (November–February) are generally wetter than the March baseline, summer months (May–September) are characterized by surficial drying, especially in the WMF domain of the slope (Figure 8). The majority of moisture dynamics occur within the upper 2–3 m bgl with variations from the baseline ranging on average between −20% and +40% and reaching maxima of −120% and +80%, highlighting significant drying out in summer months and wetting in winter (for maximum and minimum observed GMCs, see Figure S2 in the supporting information). In deeper layers, moisture variations are significantly smaller and remain largely below ±10%. Exceptions to this are the seasonally varying GMCs imaged toward the head and toe of the slope, with the most pronounced changes occurring at the toe. Variations of the regional groundwater table are likely to cause the dynamics at the toe [*Uhlemann et al.*, 2016b]. Similarly, a perched aquifer at the head of the slope (mainly as a result of moisture ingress from the DF) is likely to cause the deeper dynamics imaged at the head of the slope. Just below the back scarp an area of significant surficial wetting can frequently be observed. This coincides with field observations of a sag pond occurring in this area. The GMC time series shows that the sag pond develops during winter rainfall and remains wet until late in the summer. Surface drying occurs

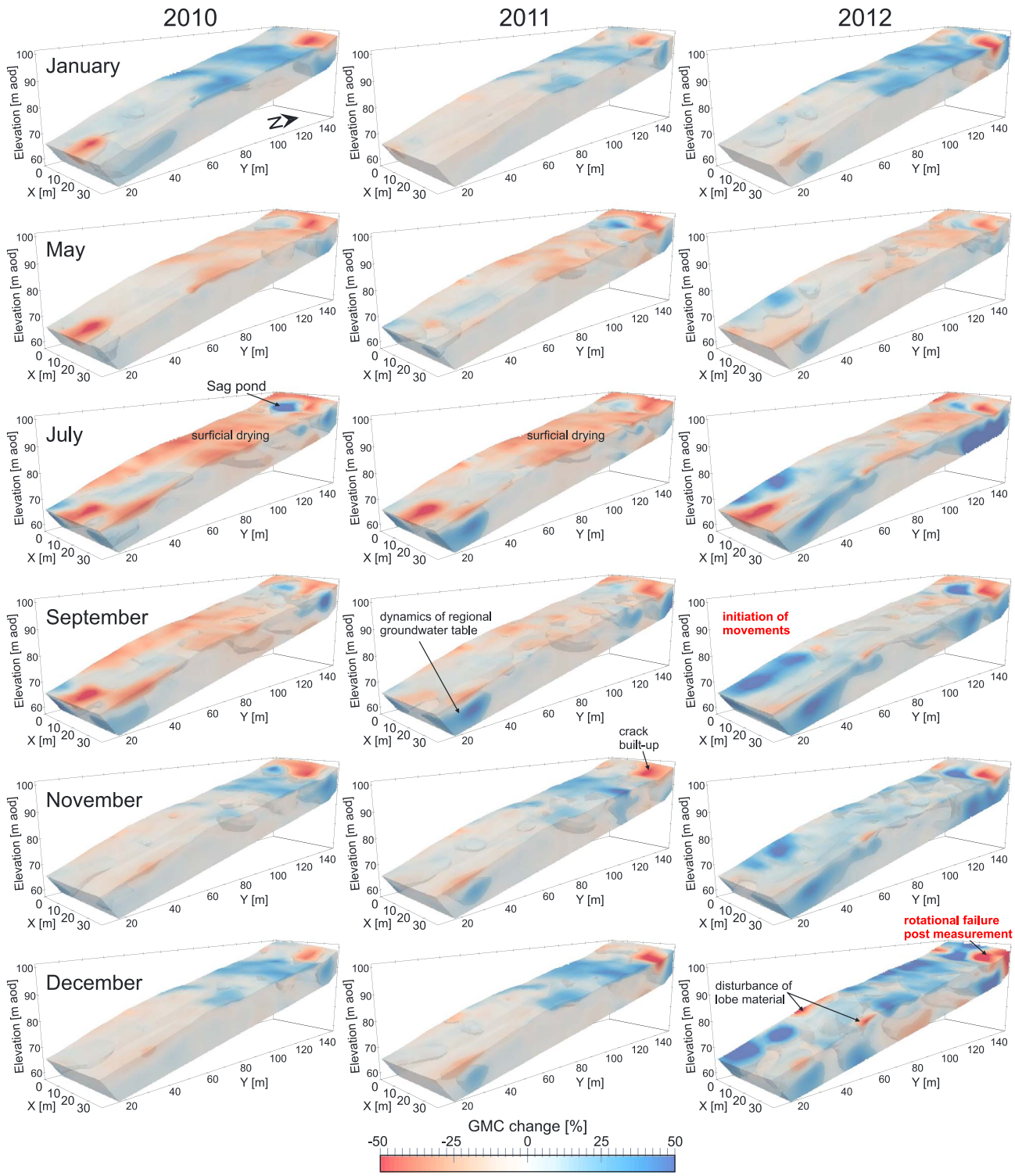

Figure 8. Change in GMC from baseline model (Figure 7). Red colors indicate a relative drying, while blue colors indicate wetting; opaque subvolumes highlight the areas where moisture contents change by more than ±10%. The years 2010 and 2011 show the typical seasonal characteristics: surficial wetting following prolonged winter rainfall (November–March) and surficial drying during the summer months (May–September). Deeper wetting fronts at the base of the slope are indicative of regional groundwater dynamics, while an area of surficial wetting close to the top of the hill coincides with a known location of a sag pond. In contrast, moisture levels in 2012 are generally higher than imaged in previous years, especially in deeper parts of the back scarp and areas of the WMF. Strongly decreasing moisture contents in parts of the lobes and back scarp indicate disturbances of the corresponding material, leading to higher crack volume and hence lower bulk GMC. Only the upper 12 m bgl of the model is shown, corresponding to the depth of the most significant GMC changes. Figure S3 in the supporting information shows a subset of the data presented here from a different viewpoint and as transects through the model.

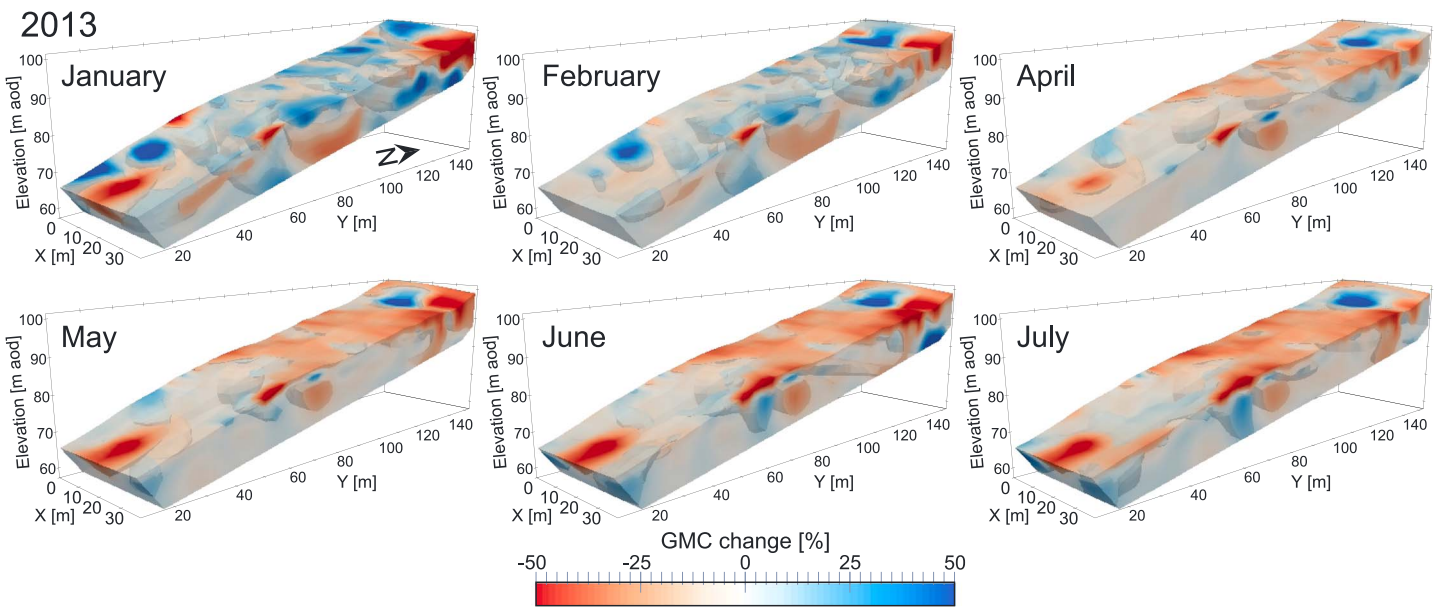

Figure 9. Change in GMC from the baseline model of March 2010 for measurement postlandslide reactivation in December 2012. Note that significant movements of up to 3.5 m occurred during December 2012 to January 2013 at the back scarp and eastern lobe. Figure S4 in the supporting information shows the data presented in this figure from a different viewpoint and as transects through the model.

during summer and is most pronounced in the upper part of the slope where the WMF is outcropping. The smaller amplitude of surface drying in the SSF is likely to be related to downslope movements of moisture accumulated in the WMF during the winter months [*Chambers et al.*, 2011]. In the back scarp a feature displaying a consistently lower GMC than at the baseline measurement can be observed; its GMC shows a decreasing trend with time. This feature is most pronounced after the summer months, while becoming wetter during winter, and is likely to be an effect of desiccation crack dynamics in the back scarp.

In comparison to 2010/2011, 2012 shows a change in these seasonal characteristics, with less surface drying in summer and significantly higher GMCs throughout the year, peaking prior to reactivation and failure in late December 2012. Higher GMCs can already be observed in January, as a result of prolonged rainfall in November and December 2011 (Figure 3). The wet spring and summer of 2012 interrupted the surface drying that was observed in the previous years. The moist anomalies at the head and toe of the slope show their largest extent and amplitudes in July and September 2012, indicative of a significant rise in the regional groundwater table. From September to December 2012, a continuous increase in moisture content can be observed in the upper 3 m bgl, highlighting increased moisture infiltration as a result of prolonged and intense rainfall. Despite the general increase in moisture content, the lobes and back scarp, i.e., areas of instability, show a generally decreasing trend. This may be a result of disturbance of the material, resulting in an increasing amount of macropores due to soil-cracking and/or shrink-swell processes, and thus improved drainage of surface waters into deeper layers through preferential flow [*Krzeminska et al.*, 2012; *Lu and Godt*, 2013]. This process is indicated by areas of increased moisture content reaching from above to below these features, in particular at the western lobe.

4.3. Moisture Dynamic Post Reactivation

Moisture levels decreased after the reactivation of December 2012, where between December 2012 and January 2013 surface movements of up to 3.5 m occurred along the back scarp and eastern lobe. In January and February 2013 GMCs were still elevated but with a decreasing trend (Figure 9). The spatially continuous, shallow moist layer that can be observed in December 2012 gradually loses its continuity in the early months of 2013. In February, GMCs have noticeably decreased, and only patches of elevated moisture content remain, highlighting the heterogeneity of the material where moisture remains in areas of particularly low permeability, while draining through cracks and fissures in other parts. Noticeably greater moisture remains in the WMF, while large parts of the SSF show moisture levels close to the baseline measurement,

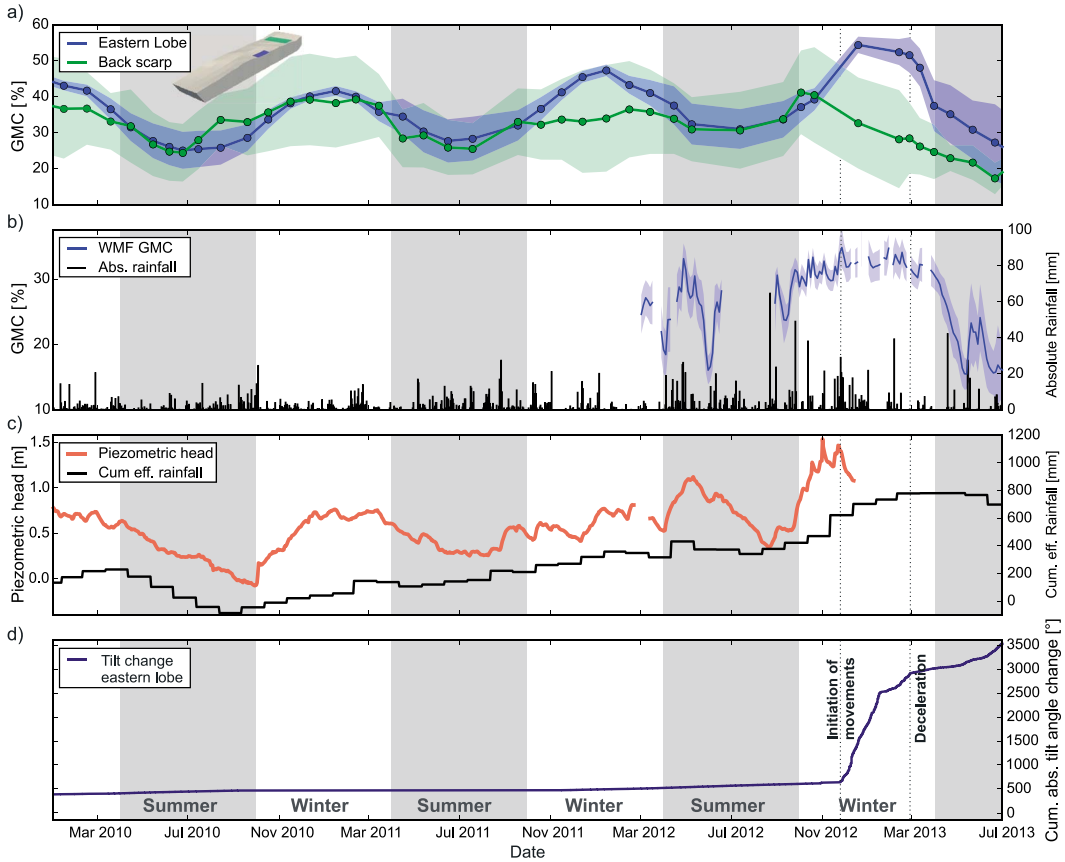

Figure 10. (a) ERI-derived GMC time series characteristic for shallow parts of the eastern lobe and back scarp. Shaded areas indicate the standard deviation of these values. (b) GMC data recorded in the central part of the WMF using Decagon 5TE sensors; shaded areas indicate the standard deviation. The absolute daily rainfall is also shown. (c) Piezometric head measured on the eastern lobe and cumulative effective monthly rainfall, highlighting the positive water balance of 2011 and 2012. (d) Cumulative absolute change in tiltmeter reading, highlighting the onset of slope instabilities in December 2012.

highlighting the higher permeability and thus drainage potential of this formation. Comparing the results of December 2012 with January 2013, a considerable decrease in GMC in the failed area of the eastern part of the back scarp is found. This can be explained by an opening of drainage pathways, and perhaps surface drainage, as a result of the rotational failure.

From April 2013 onward, GMCs decreased throughout the slope and in the WMF in particular (Figure 10a). The drying patterns are comparable to features observed in the summers of 2010/2011. While the WMF, including the material of the lobes, showed significant decreases in GMC to depths of 3 m bgl, potential moisture ingress from the DF accumulates just below the back scarp resulting in the buildup of a sag pond. Moisture pathways, allowing for drainage from the upper parts of the slope, are becoming evident in the SSF in July 2013 (Figures 11 and S3). These pathways correlate with results of *Chambers et al.* [2011], where self-potential mapping indicated flow of moisture from the WMF into the central part of the SSF. Despite movements of up to 3.5 m, which has a significant impact on the ERI imaging array, using the reported methodology made it possible to image moisture dynamics prior to and post landslide reactivation virtually without any artifacts resulting from these movements.

5. Discussion

ERI monitoring can provide volumetric images of the GMC distribution in the slope over time. However, it only provides an indirect measurement of GMC. Thus, these indirect measurements were compared to other direct observations of moisture content, piezometric head, and rainfall (Figure 10); all of which provide

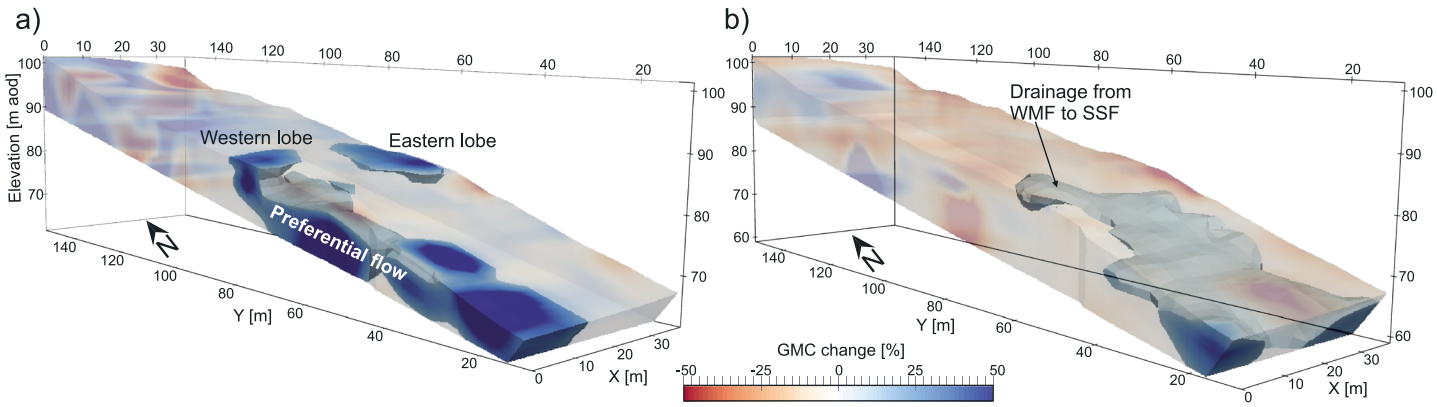

Figure 11. (a) Data of December 2012 showing preferential flow at the western lobe during reactivation of the landslide. Flow paths are imaged at a depth of about 5 m bgl, diverting moisture from the shear surface, maintaining low pore pressures. This process is not occurring at the eastern lobe, which subsequently showed movements of up to 3.5 m. (b) Data of July 2013 highlighting preferential flowpaths allowing for moisture movement from the WMF to the SSF.

information on the saturation state of the slope. For this comparison, average GMC values were extracted from the models at areas characteristic for the shallow dynamics of the eastern lobe and back scarp (Figure 10a). Although only available from February 2012, GMC was monitored at discrete points within the WMF (locations shown in Figure 2) at depths of about 0.1 m bgl using commercial point probes (Decagon 5TE). Figure 10b shows the average of data obtained from seven probes. Those point measurements show an increasing trend from February 2012 to January 2013, after which GMCs rapidly declined; a similar trend can be observed in the ERI-derived GMC data of the eastern lobe. Values of the point sensors vary between 15% and 35% and are thus within the same order as the ERI-derived GMCs. However, the sensor data show significantly more variability, which is caused by a higher sampling frequency (daily versus monthly), very shallow installation of these sensors, and sampling of considerably smaller volumes than obtained with ERI.

Moderate to strong correlation was determined between piezometric head (Figure 10c) and ERI-derived GMC, with Pearson's $r = 0.61$ and 0.58 for the correlation with the data of the eastern lobe and back scarp, respectively. Figure 10c also shows the monthly cumulative effective rainfall recorded over the monitoring period. In summer 2010 a value of 0 is reached, indicating a maintained water balance. The comparatively wet summers 2011 and 2012 resulted in a positive water balance, where moisture intake overcomes the moisture loss due to evapotranspiration. This resulted in the overall rise in moisture content that was imaged in 2011 and peaking in 2012 (Figures 8 and 10c) and explains the continuous rise in piezometric head. This correlation between independent direct observations of saturation state and ERI-derived GMCs highlights the reliability of the presented approach. Nevertheless, ERI provides volumetric resistivity distributions over time, which are only a proxy for the GMC distributions. By correcting for seasonal variations in temperature, and assuming that the characteristic resistivity of the materials and pore fluids remain constant, resistivity can directly be related to GMC (equation (3)). This relation may break down if considerable changes in material or pore fluid composition occur.

The spatial and temporal moisture dynamics highlight the seasonal flow of water in the slope. Moisture, which accumulated during winter months, drains from May to September from the base of the WMF into the underlying SSF. This groundwater discharge is focused in the center of the slope at about 3 m bgl, following the local topography. From this discharge point, water spreads out while flowing downhill and reaches the surface toward the toe of the slope. This characteristic summer drainage was observed not only prior to reactivation but also post reactivation, highlighting that the moisture pathways leading to this flow pattern were not disturbed during the landslide movements. In contrast to the focused, deeper discharge of moisture from the WMF into the SSF, moisture accumulation in the upper parts of the slope mainly occurs in the upper 1 m bgl. The majority of moisture accumulates in December to February between $y = 90$ m and 130 m (Figure S5), a region which also has the smallest slope angle at site due to the formation of terraces. The distance between the area of accumulation and drainage is about 35 m. Taking into account the start of moisture accumulation (December) and drainage (July), a hydraulic conductivity for the WMF of 1.9×10^{-6} m/s can be estimated, which

is within the characteristic range for mixtures of sands, silts, and weathered clays and in agreement with earlier studies on the hydraulic conductivity of Lias Group rocks and soils [*Hobbs et al*., 2012] and UK clays in general [*Glendinning et al*., 2014].

Relating the onset of landslide movements with the imaged GMCs, a triggering threshold of $GMC_{thres} = 49\%$ can be defined at the eastern lobe (Figures 10a and 10d). This value is in the range within which the liquid limit of the WMF is found [*Hobbs et al*., 2012]. Movements of up to 3.5 m occurred between December 2012 and January 2013, followed by smaller movements until the beginning of March 2013, after which slope movements became very slow. This period of deceleration coincides with the time at which the imaged GMC of the eastern lobe falls below the threshold, highlighting its applicability. Thus, a GMC threshold obtained from ERI-derived GMCs potentially provides a more robust warning limit than thresholds solely defined on rainfall intensities. This is principally because GMC-derived thresholds account for the infiltrated moisture, and thus the saturation state, which cannot be assessed by rainfall values only [*Godt et al*., 2006, 2009]. Note that the most intense rainfall was recorded in September 2012 and not in December when movements started, which would have triggered a false alarm using the majority of rainfall threshold approaches.

Despite previously exhibiting the greatest activity on the slope, the western lobe remained largely stable during this reactivation of December 2012 (Figure 3). This can be explained by preferential flow through the aeolian sand deposits and surface fissures leading to drainage of water from the upper part of the western lobe to below it (Figure 11a). Moisture content and thus pore pressures at the critical depth therefore remained at a significantly lower level compared to the eastern lobe. This flow through a highly permeable layer has recently been confirmed when movements in the western lobe potentially blocked these paths, causing rapid elevations in piezometric head (e.g., 1 m in 2 days) during saturated winter conditions. Heterogeneous hydrological conditions, and preferential flow in particular, are known to affect landslide movements. They can increase or decrease slope stability. An increase in effective stress through moisture drainage away from the sliding surface will act as a stabilizing force, while decreasing effective stress through water accumulation above the sliding surface may lead to failure [*Uchida et al*., 2001; *Krzeminska et al*., 2012, 2013; *Bogner et al*., 2014; *Anagnostopoulos et al*., 2015]; both effects were observed at Hollin Hill. Preferential flow is interpreted to cause the relative decrease in shallow GMCs in the back scarp, where drainage into deeper layers occurs through tension cracks and fissures. These were observed prior to the rotational failure in December 2012. From the GMC time series, the rotational failure can be explained by material softening through cycling between wet and dry states prior to the failure [*Take and Bolton*, 2011], and high pore pressures as a result of high moisture contents at the toe of this slip, resulting in reduced effective stress, shear strength, and hence stability. However, the resolution of the ERI array is not sufficient to image details of the processes causing the rotational failure.

The GMC models demonstrated that the highest-amplitude moisture dynamics took place at depths above 2–3 m bgl (Figures S5–S7). This coincides with the depth at which shear surfaces have been found and indicates that wetting and drying cycles, leading to material softening, are one of the drivers for the instabilities. The rapid acceleration of lobe movements can be explained by the exceptionally wet state of the slope during the reactivation (Figures S5 and S6), elevating pore pressures at the preexisting shear surface, reducing effective stress, shear strength, thus causing instabilities. With the dissipation of moisture into deeper layers in January and February 2012, pore pressures were declining and so effective stress and shear strength increased again, resulting in smaller movements. It is evident from the time series (Figure 10) that a certain moisture level is indicative of pore pressures at critical depths that are causing movements. This information, and also the comparison to the western lobe where only minimal movements were observed, can be used in the design of remediation measures. For example, installing a vertical drain on the top of the eastern lobe, allowing moisture to flow from the WMF into the SSF, would stabilize this lobe by reducing pore pressures and thus keeping effective stress and shear strength at higher levels during periods of prolonged and intense rainfall.

During the monitoring period significant movements of the order of the electrode spacing occurred at Hollin Hill. Figure 1 shows that this magnitude of movements causes distortions in the resistivity models of more than 40%, which would have masked the imaged GMC changes. Using the proposed methodology, imaging of GMC virtually without artifacts was possible despite these significant movements and allowed for an interpretation of the hydrological processes characterizing the reactivation. This highlights the need to account for changing electrode positions and also shows why this has recently become a

research focus [*Wilkinson et al*., 2010, 2015, 2016; *Kim et al*., 2014; *Loke et al*., 2015]. This is the first study that successfully employs moving electrode positions within an ERI monitoring methodology.

The presented approach has two main limitations. Despite recent advances in 4-D ERI data inversion [*Kim et al*., 2009, 2013; *Karaoulis et al*., 2011, 2014; *Loke et al*., 2014; *Rucker*, 2014] that allow for a simultaneous inversion of all time steps, thereby providing more robust ERI monitoring results [*Power et al*., 2014], these could not be implemented in this study. This is because these algorithms require electrode positions to be constant over time. But despite not using these more advanced inversion methods, it was possible to obtain reliable results that are in agreement with independent observations. Another limitation is the assumption that the surface topography remains unchanged during movements. In the case of Hollin Hill, changes in surface topography are typically less than 0.25 m in vertical extent and mainly restricted to the movements of the lobes and back scarp. Although not considering an actual change in surface topography, *Wilkinson et al*. [2015] argued that the sensitivity of ERI to vertical electrode movements would be small, provided that significant changes in local topography did not occur. Thus, only small distortions in the resulting resistivity and GMC distributions can be expected when not accounting for the changes in surface topography.

The extension from 2-D sections to 3-D volumes will open new opportunities in landslide research and equip geotechnical engineers and engineering geologists with a volumetric and time-varying moisture distribution in slopes, which will have significant benefits for slope stability analysis [*Bogaard and Greco*, 2016]. Yet ERI data analysis requires a significant amount of manual data preparation and analysis. This manual processing is likely to be minimized by further advances in automated interpretation of ERI models that allow for tracking of moisture fronts and groundwater dynamics [*Chambers et al*., 2015; *Ward et al*., 2016]. Once these steps form a standard part of the ERI data processing workflow, GMC dynamics can be imaged quickly and robustly. This will enable the incorporation of ERI monitoring into early-warning systems that can provide reliable alarms to endangered communities and assets [*Lacasse and Nadim*, 2009; *Michoud et al*., 2013], by informing about the historic and present moisture contents and pore pressures in slopes, thus mitigating their risk [*van Westen et al*., 2006; *Berti et al*., 2012; *Bogaard and Greco*, 2016]. This will provide the potential not only to define triggering thresholds but also to study the causes for landsliding and proactively provide information to facilitate the design of early and effective intervention strategies to stabilize slopes [*Crozier and Glade*, 2005; *Popescu and Sasahara*, 2009; *BSI*, 2015], which are more cost-effective than reactive remediation of failures.

6. Conclusions

Geophysical characterization has become frequently applied to landslide investigations in recent years. Although it is known that geophysical monitoring, using geoelectrical techniques in particular, has the potential to image hydrological processes, to date its application to landslide studies has been limited. By introducing a methodology to implement moving electrode positions into a time-lapse inversion workflow, this study presents the first long-term 4-D (i.e., 3-D time lapse) imaging of moisture dynamics prior to and post-landslide reactivation. Uncertainties are reduced by incorporating lithological boundaries obtained from seismic refraction data. The results show that prior to reactivation the slope exhibits characteristic seasonal behavior, with decreasing moisture content in summer and increasing GMC in winter. These changes were found to be limited to the uppermost 2–3 m bgl. In addition to this shallow behavior, deep moisture dynamics were imaged, which relate to dynamics of the regional groundwater table. The months prior to landslide reactivation exhibited a significant rise in GMC, leading to a change from the seasonal characteristics, where exceptionally high moisture levels were imaged during summer, which further increased toward winter when the movements initiated. Post reactivation, GMCs were found to decline, exhibiting complex patterns of changes indicating the formation of ponds and drainage through cracks and fissures. Toward the summer, the moisture dynamics exhibited the seasonal characteristics observed prior to reactivation. Using 4-D ERI, dynamic preferential flow paths were imaged. Despite significant movements of up to 3.5 m, the GMC models are virtually free of artifacts, highlighting the success and performance of the presented methodology. The flow dynamics observed in the 4-D moisture data showed yearly drainage of moisture from the mudstone into the sandstone formation during summer months, which accumulated in the upper parts of the slope during the months of December to February. This yearly behavior allowed an estimate of the hydraulic conductivity of the mudstone formation to be made at 1.9×10^{-6} m/s, which was shown

to be in agreement with previously published results. Being able to provide information about the temporal and spatial variations of moisture dynamics in an unstable slope is a prerequisite for a coupled hydrogeophysical-hydrogeomechanical slope modeling. In combination with near real-time delivery of geophysical monitoring data, this will allow estimation of temporally varying factors of safety for a slope and highlight likely failure mechanisms at appropriate time scales.

Having an understanding of the hydrological processes causing slope instabilities is crucial to effectively designing mitigation measures to protect communities and infrastructures at risk. Thus, ERI monitoring, as shown here, is capable of providing temporal volumetric information at a scale that is not achievable from conventional point sensors. It was shown that hydrological processes controlling landslide processes, such as soil piping, can be imaged. Based on the results a remediation measure could be proposed to limit movements. Knowing the processes causing landslide activation will improve the performance of early-warning systems, providing more reliable alarms, thereby increasing their acceptance and implementation.

Acknowledgments
In fond memory of Steve Gibson. We are hugely grateful to Steve and Josie Gibson (the landowners of Hollin Hill) for their continuous support and involvement in the research conducted at the landslide observatory throughout the years. We thank the Editor, Giovanni Coco, the Associate Editor, Joel Johnson, Dale Rucker, and two anonymous reviewers for their fruitful comments. We would also like to thank Colm Jordan for the provision of the DEM data, Carl Watson for providing the point-sensor soil moisture data, and Tim Johnson for advice and support with E4D. The Natural Environment Research Council (NERC) supported this research. This paper is published with the permission of the Executive Director of the British Geological Survey (NERC). The analyzed data are archived by the British Geological Survey and are available from the authors. For data access, please contact Sebastian Uhlemann (suhl@bgs.ac.uk).

References

Allison, R. J., and D. Brunsden (1990), Some mudslide movement patterns, *Earth Surf. Process. Landforms*, *15*, 297–311, doi:10.1002/esp.3290150402.

Anagnostopoulos, G. G., S. Fatichi, and P. Burlando (2015), An advanced process-based distributed model for the investigation of rainfall-induced landslides: The effect of process representation and boundary conditions, *Water Resour. Res.*, *51*, 7501–7523, doi:10.1002/2015WR016909.

Belcher, S., et al. (2014), *Too Hot, Too Cold, Too Wet, Too Dry: Drivers and Impacts of Seasonal Weather in the UK*, Met Office, Exeter, U. K.

Benisch, K., D. Köhn, S. al Hagrey, W. Rabbel, and S. Bauer (2015), A combined seismic and geoelectrical monitoring approach for CO_2 storage using a synthetic field site, *Environ. Earth Sci.*, *73*(7), 3077–3094, doi:10.1007/s12665-014-3603-0.

Bergmann, P., M. Ivandic, B. Norden, C. Rücker, D. Kiessling, S. Lüth, C. Schmidt-Hattenberger, and C. Juhlin (2014), Combination of seismic reflection and constrained resistivity inversion with an application to 4D imaging of the CO_2 storage site, Ketzin, Germany, *Geophysics*, *79*(2), B37–B50, doi:10.1190/geo2013-0131.1.

Berti, M., M. L. V. Martina, S. Franceschini, S. Pignone, A. Simoni, and M. Pizziolo (2012), Probabilistic rainfall thresholds for landslide occurrence using a Bayesian approach, *J. Geophys. Res.*, *117*, F04006, doi:10.1029/2012JF002367.

Binley, A., S. S. Hubbard, J. A. Huisman, A. Revil, D. A. Robinson, K. Singha, and L. D. Slater (2015), The emergence of hydrogeophysics for improved understanding of subsurface processes over multiple scales, *Water Resour. Res.*, *51*, 3837–3866, doi:10.1002/2015WR017016.

Bishop, A. W., and L. Bjerrum (1960), *The Principle of Effective Stress*, Norges Geotekniske Inst, Oslo.

Bogaard, T. A., and R. Greco (2016), Landslide hydrology: From hydrology to pore pressure, *Wiley Interdiscip. Rev. Water*, *3*(3), 439–459, doi:10.1002/wat2.1126.

Bogner, C., F. Bauer, B. Trancóny, P. Widemann, L. B. Viñan, and B. Huwe (2014), Quantifying the morphology of flow patterns in landslide-affected and unaffected soils, *J. Hydrol.*, *511*, 460–473, doi:10.1016/j.jhydrol.2014.01.063.

Bordoni, M., C. Meisina, R. Valentino, N. Lu, M. Bittelli, and S. Chersich (2015), Hydrological factors affecting rainfall-induced shallow landslides: From the field monitoring to a simplified slope stability analysis, *Eng. Geol.*, *193*, 19–37, doi:10.1016/j.enggeo.2015.04.006.

Brunet, P., R. Clément, and C. Bouvier (2010), Monitoring soil water content and deficit using electrical resistivity tomography (ERT)—A case study in the Cevennes area, France, *J. Hydrol.*, *380*(1–2), 146–153, doi:10.1016/j.jhydrol.2009.10.032.

BSI (2015), Code of practice for ground investigations, BS 5930:2015, United Kingdom.

Chambers, J. E., P. B. Wilkinson, O. Kuras, J. R. Ford, D. A. Gunn, P. I. Meldrum, C. V. L. Pennington, A. L. Weller, P. R. N. Hobbs, and R. D. Ogilvy (2011), Three-dimensional geophysical anatomy of an active landslide in Lias Group mudrocks, Cleveland Basin, UK, *Geomorphology*, *125*(4), 472–484, doi:10.1016/j.geomorph.2010.09.017.

Chambers, J. E., D. A. Gunn, P. B. Wilkinson, P. I. Meldrum, E. Haslam, S. Holyoake, M. Kirkham, O. Kuras, A. Merritt, and J. Wragg (2014), 4D electrical resistivity tomography monitoring of soil moisture dynamics in an operational railway embankment, *Near Surf. Geophys.*, *12*(2007), 61–72, doi:10.3997/1873-0604.2013002.

Chambers, J. E., et al. (2015), Spatial monitoring of groundwater drawdown and rebound associated with quarry dewatering using automated time-lapse electrical resistivity tomography and distribution guided clustering, *Eng. Geol.*, *193*, 412–420, doi:10.1016/j.enggeo.2015.05.015.

Chrétien, M., J. F. Lataste, R. Fabre, and A. Denis (2014), Electrical resistivity tomography to understand clay behavior during seasonal water content variations, *Eng. Geol.*, *169*, 112–123, doi:10.1016/j.enggeo.2013.11.019.

Corsini, A., A. Pasuto, M. Soldati, and A. Zannoni (2005), Field monitoring of the Corvara landslide (Dolomites, Italy) and its relevance for hazard assessment, *Geomorphology*, *66*(1–4), 149–165, doi:10.1016/j.geomorph.2004.09.012.

Crozier, M. J., and T. Glade (2005), Landslide hazard and risk: Issues, concepts and approach, in *Landslide Hazard and Risk*, edited by T. Glade, M. Anderson, and M. J. Crozier, pp. 1–40, John Wiley, Chichester, West Sussex, U. K.

Cruden, D. M., and D. J. Varnes (1996), Landslide types and processes, in *Landslides Investigation Mitigation*, *Spec. Rep.*, vol. 247, edited by A. K. Turner et al., pp. 36–75, National Academy Press, Washington, D. C.

Daily, W., A. Ramirez, and A. Binley (2004), Remote monitoring of leaks in storage tanks using electrical resistance tomography: Application at the Hanford Site, *J. Environ. Eng. Geophys.*, *9*(1), 11–24, doi:10.4133/JEEG9.1.11.

Dijkstra, T. A., and N. Dixon (2010), Climate change and slope stability in the UK: Challenges and approaches, *Q. J. Eng. Geol. Hydrogeol.*, *43*(4), 371–385, doi:10.1144/1470-9236/09-036.

Dijkstra, T., N. Dixon, C. Crosby, M. Frost, D. Gunn, P. Fleming, and J. Wilks (2014), Forecasting infrastructure resilience to climate change, *Proc. Inst. Civ. Eng.*, *167*(TR5), 269–280, doi:10.1680/tran.13.00089.

Dixon, N., M. P. Spriggs, A. Smith, P. Meldrum, and E. Haslam (2014), Quantification of reactivated landslide behaviour using acoustic emission monitoring, *Landslides*, *12*(3), 549–560, doi:10.1007/s10346-014-0491-z.

Doetsch, J., N. Linde, M. Pessognelli, A. G. Green, and T. Günther (2012), Constraining 3-D electrical resistance tomography with GPR reflection data for improved aquifer characterization, *J. Appl. Geophys.*, *78*, 68–76, doi:10.1016/j.jappgeo.2011.04.008.

Foster, C., G. O. Jenkins, and A. D. Gibson (2007), *Landslides and Mass Movement Processes and Their Distribution in the York District (Sheet 63)*, British Geol. Surv, Keyworth, U. K.

Gance, J., J.-P. Malet, R. Supper, P. Sailhac, D. Ottowitz, and B. Jochum (2016), Permanent electrical resistivity measurements for monitoring water circulation in clayey landslides, *J. Appl. Geophys.*, *126*, 98–115, doi:10.1016/j.jappgeo.2016.01.011.

Gasmo, J. M., H. Rahardjo, and E. C. Leong (2000), Infiltration effects on stability of a residual soil slope, *Comput. Geotech.*, *26*(2), 145–165, doi:10.1016/S0266-352X(99)00035-X.

Gaunt, G. D., H. C. Ivimey-Cook, I. E. Penn, and B. M. Cox (1980), *Mesozoic Rocks Proved by IGS Boreholes in the Humber and Acklam Areas*, Institute of Geological Studies, Nottingham, U. K.

Gibson, A. D., M. G. Culshaw, C. Dashwood, and C. V. L. Pennington (2013), Landslide management in the UK—The problem of managing hazards in a "low-risk" environment, *Landslides*, *10*(5), 599–610, doi:10.1007/s10346-012-0346-4.

Glendinning, S., P. Hughes, P. Helm, J. Chambers, J. Mendes, D. Gunn, P. Wilkinson, and S. Uhlemann (2014), Construction, management and maintenance of embankments used for road and rail infrastructure: Implications of weather induced pore water pressures, *Acta Geotech.*, *9*(5), 799–816, doi:10.1007/s11440-014-0324-1.

Glendinning, S., et al. (2015), Research-informed design, management and maintenance of infrastructure slopes: Development of a multi-scalar approach, *IOP Conf. Ser. Earth Environ. Sci.*, *26*(1), 12005, doi:10.1088/1755-1315/26/1/012005.

Godt, J. W., R. L. Baum, and A. F. Chleborad (2006), Rainfall characteristics for shallow landsliding in Seattle, Washington, USA, *Earth Surf. Process. Landforms*, *31*(1), 97–110, doi:10.1002/esp.1237.

Godt, J. W., R. L. Baum, and N. Lu (2009), Landsliding in partially saturated materials, *Geophys. Res. Lett.*, *36*, L02403, doi:10.1029/2008GL035996.

Guha-Sapir, D., R. Below, and P. Hoyois (2016), EM-DAT: The CRED/OFDA International Disaster Database.

Gunn, D. A., J. E. Chambers, P. R. N. Hobbs, J. R. Ford, P. B. Wilkinson, G. O. Jenkins, and A. Merritt (2013), Rapid observations to guide the design of systems for long-term monitoring of a complex landslide in the Upper Lias clays of North Yorkshire, UK, *Q. J. Eng. Geol. Hydrogeol.*, *46*(3), 323–336, doi:10.1144/qjegh2011-028.

Hayashi, M. (2004), Temperature-electrical conductivity relation of water for environmental monitoring and geophysical data inversion, *Environ. Monit. Assess.*, *96*, 119–128.

Hayley, K., L. R. Bentley, M. Gharibi, and M. Nightingale (2007), Low temperature dependence of electrical resistivity: Implications for near surface geophysical monitoring, *Geophys. Res. Lett.*, *34*, L18402, doi:10.1029/2007GL031124.

Highland, L., and P. Bobrowsky (2008), *The Landslide Handbook: A Guide to Understanding Landslides*, U.S. Geol, Reston, Va.

Hobbs, P. R. N., D. C. Entwisle, K. J. Northmore, M. G. Sumbler, L. D. Jones, S. Kemp, S. Self, M. Barron, and J. L. Meakin (2012), Engineering Geology of British Rocks and Soils—Lias Group, 323 pp., British Geological Survey Internal Report, Keyworth, U. K.

Huang, A.-B., J.-T. Lee, Y.-T. Ho, Y.-F. Chiu, and S.-Y. Cheng (2012), Stability monitoring of rainfall-induced deep landslides through pore pressure profile measurements, *Soils Found.*, *52*(4), 737–747, doi:10.1016/j.sandf.2012.07.013.

Johnson, T. C., R. J. Versteeg, A. Ward, F. D. Day-Lewis, and A. Revil (2010), Improved hydrogeophysical characterization and monitoring through parallel modeling and inversion of time-domain resistivity and induced-polarization data, *Geophysics*, *75*(4), WA27, doi:10.1190/1.3475513.

Jongmans, D., and S. Garambois (2007), Geophysical investigation of landslides: A review, *Bull. la Société géologique Fr.*, *33*(1), 101–112.

Karaoulis, M. C., J.-H. Kim, and P. I. Tsourlos (2011), 4D active time constrained resistivity inversion, *J. Appl. Geophys.*, *73*(1), 25–34, doi:10.1016/j.jappgeo.2010.11.002.

Karaoulis, M., P. Tsourlos, J. Kim, and A. Revil (2014), 4D time-lapse ERT inversion: Introducing combined time and space constraints, *Near Surf. Geophys.*, *12*, 1–10, doi:10.3997/1873-0604.2013004.

Kim, J. H., M. J. Yi, R. Supper, and D. Ottowitz (2014), Simultaneous inversion of resistivity structure and electrode locations in ERT, in *Near Surface Geoscience 2014*, pp. 14–18, European Association of Geoscientists and Engineers, Athens.

Kim, J.-H., M.-J. Yi, S.-G. Park, and J. G. Kim (2009), 4-D inversion of DC resistivity monitoring data acquired over a dynamically changing Earth model, *J. Appl. Geophys.*, *68*(4), 522–532, doi:10.1016/j.jappgeo.2009.03.002.

Kim, J.-H., R. Supper, P. Tsourlos, and M.-J. Yi (2013), Four-dimensional inversion of resistivity monitoring data through Lp norm minimizations, *Geophys. J. Int.*, *195*(3), 1640–1656, doi:10.1093/gji/ggt324.

Kirschbaum, D., T. Stanley, and Y. Zhou (2015), Spatial and temporal analysis of a global landslide catalog, *Geomorphology*, *249*, 4–15, doi:10.1016/j.geomorph.2015.03.016.

Krzeminska, D. M., T. A. Bogaard, T. W. J. van Asch, and L. P. H. van Beek (2012), A conceptual model of the hydrological influence of fissures on landslide activity, *Hydrol. Earth Syst. Sci.*, *16*(6), 1561–1576, doi:10.5194/hess-16-1561-2012.

Krzeminska, D. M., T. A. Bogaard, J.-P. Malet, and L. P. H. van Beek (2013), A model of hydrological and mechanical feedbacks of preferential fissure flow in a slow-moving landslide, *Hydrol. Earth Syst. Sci.*, *17*(3), 947–959, doi:10.5194/hess-17-947-2013.

Kuras, O., J. D. Pritchard, P. I. Meldrum, J. E. Chambers, P. B. Wilkinson, R. D. Ogilvy, and G. P. Wealthall (2009), Monitoring hydraulic processes with automated time-lapse electrical resistivity tomography (ALERT), *C. R. Geosci.*, *341*(10–11), 868–885, doi:10.1016/j.crte.2009.07.010.

LaBrecque, D. J., and X. Yang (2001), Difference inversion of ERT data: A fast inversion method for 3-D in situ monitoring, *J. Environ. Eng. Geophys.*, *6*(2), 83–89, doi:10.4133/JEEG6.2.83.

LaBrecque, D. J., M. Miletto, W. Daily, A. Ramirez, and E. Owen (1996), The effects of noise on Occam's inversion of resistivity tomography data, *Geophysics*, *61*(2), 538–548.

Lacasse, S., and F. Nadim (2009), Landslide risk assessment and mitigation strategy, in *Landslides—Disaster Risk Reduction*, edited by K. Sassa and P. Canuti, pp. 31–61, Springer, Berlin Heidelberg.

Lehmann, P., F. Gambazzi, B. Suski, L. Baron, A. Askarinejad, S. M. Springman, K. Holliger, and D. Or (2013), Evolution of soil wetting patterns preceding a hydrologically induced landslide inferred from electrical resistivity survey and point measurements of volumetric water content and pore water pressure, *Water Resour. Res.*, *49*, 7992–8004, doi:10.1002/2013WR014560.

Loke, M. H. (2001), Constrained time-lapse resistivity imaging inversion, in *Symposium on the Application of Geophysics to Engineering and Environmental Problems 2001*, pp. EEM7–EEM7 , Environ. and Eng. Geophys. Soc, Denver, Colo.

Loke, M. H., J. E. Chambers, D. F. Rucker, O. Kuras, and P. B. Wilkinson (2013), Recent developments in the direct-current geoelectrical imaging method, *J. Appl. Geophys.*, *95*, 135–156, doi:10.1016/j.jappgeo.2013.02.017.

Loke, M. H., T. Dahlin, and D. F. Rucker (2014), Smoothness-constrained time-lapse inversion of data from 3D resistivity surveys, *Near Surf. Geophys.*, *12*(2007), 5–24, doi:10.3997/1873-0604.2013025.

Loke, M. H., P. B. Wilkinson, and J. E. Chambers (2015), Rapid inversion of data from 2-D and from 3-D resistivity surveys with shifted electrodes, pp. 6–10.

Lu, N., and J. W. Godt (2013), *Hillslope Hydrology and Stability*, Cambridge Univ. Press, Cambridge, U. K.

Lu, N., J. W. Godt, and D. T. Wu (2010), A closed-form equation for effective stress in unsaturated soil, *Water Resour. Res.*, *46*, W05515, doi:10.1029/2009WR008646.

Ma, R., A. McBratney, B. Whelan, B. Minasny, and M. Short (2011), Comparing temperature correction models for soil electrical conductivity measurement, *Precis. Agric.*, *12*(1), 55–66, doi:10.1007/s11119-009-9156-7.

Malet, J.-P., O. Maquaire, and E. Calais (2002), The use of Global Positioning System techniques for the continuous monitoring of landslides: Application to the Super-Sauze earthflow (Alpes-de-Haute-Provence, France), *Geomorphology*, *43*(1–2), 33–54, doi:10.1016/S0169-555X(01)00098-8.

Malet, J.-P., T. W. J. van Asch, R. van Beek, and O. Maquaire (2005), Forecasting the behaviour of complex landslides with a spatially distributed hydrological model, *Nat. Hazards Earth Syst. Sci.*, *5*(1), 71–85, doi:10.5194/nhess-5-71-2005.

Merritt, A. J., J. E. Chambers, W. Murphy, P. B. Wilkinson, L. J. West, D. A. Gunn, P. I. Meldrum, M. Kirkham, and N. Dixon (2013), 3D ground model development for an active landslide in Lias mudrocks using geophysical, remote sensing and geotechnical methods, *Landslides*, *11*(4), 537–550, doi:10.1007/s10346-013-0409-1.

Merritt, A. J., J. E. Chambers, P. B. Wilkinson, L. J. West, W. Murphy, D. Gunn, and S. Uhlemann (2016), Measurement and modelling of moisture—Electrical resistivity relationship of fine-grained unsaturated soils and electrical anisotropy, *J. Appl. Geophys.*, *124*, 155–165, doi:10.1016/j.jappgeo.2015.11.005.

Michoud, C., S. Bazin, L. H. Blikra, M.-H. Derron, and M. Jaboyedoff (2013), Experiences from site-specific landslide early warning systems, *Nat. Hazards Earth Syst. Sci.*, *13*(10), 2659–2673, doi:10.5194/nhess-13-2659-2013.

Mora, P., P. Baldi, G. Casula, M. Fabris, M. Ghirotti, E. Mazzini, and A. Pesci (2003), Global Positioning Systems and digital photogrammetry for the monitoring of mass movements: Application to the Ca' di Malta landslide (northern Apennines, Italy), *Eng. Geol.*, *68*(1–2), 103–121, doi:10.1016/S0013-7952(02)00200-4.

Network Rail (2014), *Route Weather Resilience and Climate Change Adaptation Plans*, Network Rail, London.

Oldenborger, G. A., P. S. Routh, and M. D. Knoll (2005), Sensitivity of electrical resistivity tomography data to electrode position errors, *Geophys. J. Int.*, *163*(1), 1–9.

Pennington, C. V. L., and A. M. Harrison (2013), 2012—Landslide year? Was the increase in UK landslides during 2012 real or apparent?, *Geosci. Mag.*, *23*(5), 10–15.

Pennington, C., K. Freeborough, C. Dashwood, T. Dijkstra, and K. Lawrie (2015), The National Landslide Database of Great Britain: Acquisition, communication and the role of social media, *Geomorphology*, doi:10.1016/j.geomorph.2015.03.013.

Perrone, A., V. Lapenna, and S. Piscitelli (2014), Electrical resistivity tomography technique for landslide investigation: A review, *Earth Sci. Rev.*, *135*, 65–82, doi:10.1016/j.earscirev.2014.04.002.

Petley, D. N., F. Mantovani, M. H. Bulmer, and A. Zannoni (2005), The use of surface monitoring data for the interpretation of landslide movement patterns, *Geomorphology*, *66*, 133–147, doi:10.1016/j.geomorph.2004.09.011.

Popescu, M. E., and K. Sasahara (2009), Engineering measures for landslide disaster mitigation, in *Landslides—Disaster Risk Reduction*, edited by K. Sassa and P. Canuti, pp. 609–631, Springer, Berlin Heidelberg.

Power, C., J. I. Gerhard, M. Karaoulis, P. Tsourlos, and A. Giannopoulos (2014), Evaluating four-dimensional time-lapse electrical resistivity tomography for monitoring DNAPL source zone remediation, *J. Contam. Hydrol.*, *162–163*, 27–46, doi:10.1016/j.jconhyd.2014.04.004.

Rucker, D. (2014), Investigating motion blur and temporal aliasing from time-lapse electrical resistivity, *J. Appl. Geophys.*, *111*, 1–13, doi:10.1016/j.jappgeo.2014.09.010.

Schwartz, B. F., M. E. Schreiber, and T. Yan (2008), Quantifying field-scale soil moisture using electrical resistivity imaging, *J. Hydrol.*, *362*(3–4), 234–246, doi:10.1016/j.jhydrol.2008.08.027.

Simeoni, L., and L. Mongiovì (2007), Inclinometer monitoring of the Castelrotto landslide in Italy, *J. Geotech. Geoenviron. Eng.*, *133*, 653–666, doi:10.1061/(ASCE)1090-0241(2007)133:6(653).

Smith, A., and N. Dixon (2015), Quantification of landslide velocity from active waveguide-generated acoustic emission, *Can. Geotech. J.*, *52*, 413–425, doi:10.1139/cgj-2014-0226.

Smith, A., N. Dixon, P. Meldrum, E. Haslam, and J. Chambers (2014), Acoustic emission monitoring of a soil slope: Comparisons with continuous deformation measurements, *Geotech. Lett.*, *4*, 255–261, doi:10.1680/geolett.14.00053.

Springman, S. M. M., P. Kienzler, S. Friedel, A. Thielen, P. Kienzler, and S. Friedel (2013), A long-term field study for the investigation of rainfall-induced landslides, *Geotechnique*, *63*(14), 1177–1193, doi:10.1680/geot.11.P.142.

Springman, S. M., P. Teysseire, and C. Jommi (2003), Instabilities on moraine slopes induced by loss of suction: A case history, *Geotechnique*, *53*(1), 3–10, doi:10.1680/geot.2003.53.1.3.

Supper, R., D. Ottowitz, B. Jochum, J.-H. Kim, A. Römer, I. Baron, S. Pfeiler, M. Lovisolo, S. Gruber, and F. Vecchiotti (2014), Geoelectrical monitoring: An innovative method to supplement landslide surveillance and early warning, *Near Surf. Geophys.*, *12*, 133–150, doi:10.3997/1873-0604.2013060.

Szalai, S., A. Koppán, and L. Szarka (2008), Effect of positional inaccuracies on multielectrode results, *Acta Geod. Geophys. Hungarica*, *43*(1), 33–42, doi:10.1556/AGeod.43.2008.1.3.

Take, W. A., and M. D. Bolton (2011), Seasonal ratcheting and softening in clay slopes, leading to first-time failure, *Geotechnique*, *61*(9), 757–769, doi:10.1680/geot.9.P.125.

Uchida, T., K. Kosugi, and T. Mizuyama (2001), Effects of pipeflow on hydrological process and its relation to landslide: A review of pipeflow studies in forested headwater catchments, *Hydrol. Process.*, *15*(11), 2151–2174, doi:10.1002/hyp.281.

Uhlemann, S. S., J. P. R. Sorensen, A. R. House, P. B. Wilkinson, C. Roberts, D. C. Gooddy, A. M. Binley, and J. E. Chambers (2016a), Integrated time-lapse geoelectrical imaging of wetland hydrological processes, *Water Resour. Res.*, *52*, 1607–1625, doi:10.1002/2015WR017932.

Uhlemann, S., P. B. Wilkinson, J. E. Chambers, H. Maurer, A. J. Merritt, D. A. Gunn, and P. I. Meldrum (2015), Interpolation of landslide movements to improve the accuracy of 4D geoelectrical monitoring, *J. Appl. Geophys.*, *121*, 93–105, doi:10.1016/j.jappgeo.2015.07.003.

Uhlemann, S., A. Smith, J. Chambers, N. Dixon, T. Dijkstra, E. Haslam, P. Meldrum, A. Merritt, D. Gunn, and J. Mackay (2016b), Assessment of ground-based monitoring techniques applied to landslide investigations, *Geomorphology*, *253*, 438–451, doi:10.1016/j.geomorph.2015.10.027.

Uhlemann, S., S. Hagedorn, B. Dashwood, H. Maurer, D. Gunn, T. Dijkstra, and J. Chambers (2016c), Landslide characterization using *P*- and *S*-wave seismic refraction tomography—The importance of elastic moduli, *J. Appl. Geophys.*, *134*, 64–76, doi:10.1016/j.jappgeo.2016.08.014.

van Westen, C. J., T. W. J. van Asch, and R. Soeters (2006), Landslide hazard and risk zonation—Why is it still so difficult?, *Bull. Eng. Geol. Environ.*, *65*(2), 167–184, doi:10.1007/s10064-005-0023-0.

Ward, W. O. C., P. B. Wilkinson, J. E. Chambers, H. Nilsson, O. Kuras, and L. Bai (2016), Tracking tracer motion in a 4-D electrical resistivity tomography experiment, *Water Resour. Res.*, *52*, 4078–4094, doi:10.1002/2015WR017958.

Waxman, M. H., and L. J. Smits (1968), Electrical conductivities in oil-bearing shaly sands, *Soc. Pet. Eng. J.*, *8*, 107–122.

Wilkinson, P. B., J. E. Chambers, M. Lelliott, G. P. Wealthall, and R. D. Ogilvy (2008), Extreme sensitivity of crosshole electrical resistivity tomography measurements to geometric errors, *Geophys. J. Int.*, *173*(1), 49–62, doi:10.1111/j.1365-246X.2008.03725.x.

Wilkinson, P. B., J. E. Chambers, P. I. Meldrum, D. A. Gunn, R. D. Ogilvy, and O. Kuras (2010), Predicting the movements of permanently installed electrodes on an active landslide using time-lapse geoelectrical resistivity data only, *Geophys. J. Int.*, *183*(2), 543–556, doi:10.1111/j.1365-246X.2010.04760.x.

Wilkinson, P. B., S. Uhlemann, J. E. Chambers, P. I. Meldrum, and M. H. Loke (2015), Development and testing of displacement inversion to track electrode movements on 3-D electrical resistivity tomography monitoring grids, *Geophys. J. Int.*, *200*(3), 1566–1581, doi:10.1093/gji/ggu483.

Wilkinson, P., J. Chambers, S. Uhlemann, P. Meldrum, A. Smith, N. Dixon, and M. H. Loke (2016), Reconstruction of landslide movements by inversion of 4-D electrical resistivity tomography monitoring data, *Geophys. Res. Lett.*, *43*, 1166–1174, doi:10.1002/2015GL067494.

Zhou, B., and T. Dahlin (2003), Properties and effects of measurement errors on 2D resistivity imaging surveying, *Near Surf. Geophys.*, *1*, 105–117.